Applied Composite Materials (2022) 29:2063–2094
https://doi.org/10.1007/s10443-022-10041-4

Numerical Investigation on the Influences of Processing Conditions on Damage in the CFRTP Cutting Using a Novel Elastic–plastic Damage Model

Fuji Wang[1] · Xinghai Jin[1] · Xiaonan Wang[1] · Zhenyuan Jia[1] · Boyu Zhang[1]

Received: 15 February 2022 / Accepted: 16 May 2022 /Published online: 9 August 2022

Abstract
The high quality machining of carbon fibre reinforced thermoplastics (CFRTPs) is still a considerable challenge. It is a hot research topic to discuss the influence of machining parameters on the force and damage of CFRTP workpiece by simulation method with low cost. However, in the three-dimensional (3D) cutting process of CFRTP, the dynamic elastic–plastic deformation process of the material under complex loads and the failure of different modes are involved, therefore, it is difficult to accurately simulate the cutting process including the formation of chips and damage. To solve this problem, this paper proposes a new CFRTP elastic–plastic damage model by combining the CFRTP 3D elastic–plastic model and failure criteria (consists of Hashin's criteria, Puck's criteria and the failure criteria based on strain energy density) that take into account multiple damage modes. Based on the proposed novel material constitutive model, a finite element (FE) model of the 3D orthogonal cutting of CFRTP is established. The material removal process, chip morphology and cutting force under four typical fibre orientations are predicted, and the results show that 0° fibre orientation produces C-shaped long chips, and 45° fibre orientation produces curled long chips. For the 90° and 135° fibre orientation, the chips are fragmented, and the damage is more serious. The simulation results agree well with the experimental results in terms of chip shape and cutting force, which verifies the validity of the model. Then, the effects of fibre orientation, tool rake angle, tool edge radius and cutting depth on subsurface damage and cutting force are investigated. The subsurface damage depth and cutting force maintain roughly the same trend as the machining parameters change, so reducing the cutting force helps reduce machining damage. The results of this study are helpful for designing tool structures and optimizing process parameters, which are of great significance for suppressing damage in CFRTP machining.

Keywords Carbon fibre reinforced thermoplastic (CFRTP) · Cutting process · Simulation · Elastic–plastic damage model · Subsurface damage

✉ Fuji Wang
wfjsll@dlut.edu.cn

[1] Key Laboratory for Precision and Non-Traditional Machining Technology of the Ministry of Education, School of Mechanical Engineering, Dalian University of Technology, Dalian 116024, China

1 Introduction

Fibre-reinforced polymer composites (FRPs) have attracted extensive attention in recent years due to their excellent mechanical properties, remarkable lightness in mass, strong thermal durability and corrosion-resistant performance [1–3]. In particular, carbon fibre reinforced thermoplastics (CFRTPs) also own the advantages of short molding cycle, easy to repair and reuse of waste materials [4]. These characteristics are of great assistance for the equipment to achieve performance improvement and weight reduction, and can significantly minimize the time cost and resource waste during the manufacturing. Therefore, such materials are showing great potential for adoption within the aerospace, transportation and robot fields [5, 6]. The production procedures of the CFRTP equipment mainly include laying, curing, machining and assembly. During the machining process, the edges of the cured parts are always required to be trimmed and a large number of connecting holes are generally drilled on the workpiece [7]. These trimming and drilling processes should be carefully conducted to assure that the components meet the desired dimensional tolerance, surface quality and other functional requirements during the assembly [5]. Furthermore, since the high-end equipment fabricated by CFRTPs is often subjected to extreme loads and the service environment is complex, the processing quality of the CFRTP parts is always under strict control to ensure well service reliability.

However, the machining of CFRTPs with high quality remains a considerable challenge. The CFRTP workpiece consists of fibres, matrix and interface on the micro scale, and it shows strong anisotropy and stacking features on the macro scale. These complex material composition and structural characteristics make the local failure and the damage propagation of the CFRTPs completely different from the homogeneous metals. Due to the material property variations in the various constituent phases, serious damages including fibre-matrix debonding, fibre pull-out and delamination are inevitable to occur in the machining process. In addition, the toughness of the matrix in the CFRTPs is remarkably enhanced compared with that in the carbon/epoxy composites. Therefore, the matrix is prone to plastic deformation under the push action of the tool during cutting, and the material is hard to be effectively removed and the damages could hence be further aggravated [5, 8]. These damages could seriously destroy the structural integrity of the workpiece and significantly reduce the service life of the components. In this case, to achieve low damage and high efficiency machining of thermoplastic composites, it is necessary to in-depth analyse the damage formation process and assess the influence of processing parameters on damage, and thus optimize tool geometries and cutting conditions.

Experiment is usually the most direct research method, and some studies have been conducted to explore the forces and damage response in the CFRTP machining [4, 5, 7, 9–12]. Hocheng et al. [9] experimentally assessed the influences of the feed rate, cutting speed and drill bit geometry on the drilling force and edge damage of the CFRTP workpiece. It was found that the delamination and burring were most sensitive to impetuous feed of the drill, and small point angle or more wear-resistant tools could reduce the level of damage. Kim et al. [7] investigated the hole surface quality and damage distributions of the CFRTPs by drilling the composite workpieces under various feed rates and spindle speeds. They concluded that, at the high feed rate of 0.25 mm/rev, delamination occurs at the fibre orientation of 60°-120°. Xu et al. [4] evaluated the delamination in the drilling of carbon/polyimide and carbon/PEEK composites with different cutting conditions. The results indicated that larger delamination was induced on the carbon/PEEK composite, and the delamination factor decreased with the increase of the cutting speed or the reducing of the feed rate for

both of these two materials. These studies could help to minimize the damage generated in the machining of CFRTP composites. However, the experiment is a time-consuming and costly method. Abundant composites and tremendous amounts of tests are demanded when assessing the effects of the tool geometry and processing parameter on the damage by experiment, which results in high cost and waste and low efficiency. In addition, the fibres present in the chips are potentially harmful to the experimenter. Therefore, a novel way should be developed to further analyse the damage initiation process and damage response in the machining of CFRTP composites.

Apparently, the finite element (FE) simulation is a cost-saving and environmental protection method. With the FE simulation, the parametric studies on the damage could be done conveniently by revising the input processing parameters, fibre orientation and material properties. In other words, the numerical modelling is more suitable to investigate the damage formation mechanism during the machining of composites. When simulating the composite machining with the FE method, the material model of the workpiece should be accurately defined at the initial stage [13]. Taking the carbon/epoxy composites which have similar material composition and structural features to the CFRTPs as an example, elastic material behaviour, Hashin criteria and damage evolution laws are frequently applied for the simulation of carbon/epoxy composite cutting [14, 15], drilling [16, 17] and milling [18]. Therefore, the material initial response model, damage initiation and evolution criteria for the CFRTPs should be determined to accurately characterise the material behaviour of the workpiece during the processing. At the same time, the CFRTPs possess more capability for plastic deformation and show more ductility than the carbon/epoxy composites [9], thus the plasticity of the CFRTPs and its effect on the damage formation should be considered in the material modelling process.

Based on the continuum damage mechanics (CDM) and the theory of plasticity, a few studies have developed elastic–plastic damage models for the CFRTPs to analyse the material behaviour and damage propagation [19–23]. Weeks et al. [19, 20] predicted the material responses of the angle ply CFRTP laminates by using a one-parameter plastic potential function to describe the non-linear stress–strain relations. Chen et al. [21] proposed an elastic–plastic damage model to characterise the mechanical behaviour of the CFRTP laminates, wherein the plasticity of the composite was defined by an equivalent form of a one-parameter plastic yield function and the damage was initiated based on the theory of Hashin. With this material constitutive model, they analysed the influences of the numbers of perforated holes on the stress distribution, damage progression patterns and failure sequences of the composite-metal laminates under tensile loading [22]. By developing a FE analysis model with an elastic–plastic damage model implemented, Liu et al. [23] simulated the impact behaviours of CFRTPs, and the effects of the impact energy on the load responses and damage extent were assessed. However, in these works, CFRTP workpieces were mainly subjected to uniaxial, multi-axial or impact loads, while the CFRTP three-dimensional (3D) cutting process involves the dynamic elastic–plastic deformation process of materials under complex loads and different modes of failure. Therefore, it is difficult to accurately simulate the cutting process including the formation of chips and damage. In addition, it could be indicated from previous research that the failure and damage development of the CFRTPs depend on the fibre orientation and cutting parameters, thus parametric studies should be done to optimise the processing parameters and to suppress the damage.

The main objective of this article is to in-depth analyse the damage response in the machining of CFRTPs under various processing conditions. To this aim, a 3D numerical model for the CFRTP cutting is proposed by defining a novel elastic–plastic damage model.

In this material constitutive model, the mechanical behaviours of the composites including the plasticity are characterised by utilising a plastic yield function consisting of the various stress components, and the initiation and evolution of the damage with different modes are determined based on the Hashin and Puck criteria and the CDM. Then, the orthogonal cutting of unidirectional CFRTPs under four typical fibre orientations is modelled and the cutting forces and material removal processes are predicted. These results are compared with the experimental observations to verify the FE model and the elastic–plastic damage model. Subsequently, the changes of the subsurface damage extent with the fibre orientation, tool rake angle, tool edge radius and cutting depth in the cutting of CFRTP laminates are numerically investigated using the proposed FE model.

2 Numerical Model

In this section, details of the numerical model for the CFRTP cutting including the elastic–plastic damage model, geometric model and boundary conditions are introduced.

2.1 Elastic–plastic Damage Model

The elastic–plastic damage model contains the material initial response model, damage initiation and evolution criteria. For the material constitutive model, a plastic model is designated to characterise the plastic behaviour of the CFRTPs. The commonly applied Hashin and Puck criteria that are based on material strength are adopted to predict failure with different modes, and the failure propagation is described by linear damage evolution laws. Moreover, Zenia et al. [24] successfully defined a combined elastoplastic-damage model to analyse the cutting of carbon/epoxy laminates by utilising the failure criteria developed by Ladeveze and Lubineau et al. [25, 26] on the basis of the strain energy density. Therefore, these criteria are also involved in this work to simulate the damage onset and growth.

2.1.1 Stress–strain Relationship

Generally, the CFRTPs exhibit both elastic and plastic response, and the total strain tensor $\boldsymbol{\varepsilon}$ is the sum of the elastic strain tensor $\boldsymbol{\varepsilon}^e$ and plastic strain tensor $\boldsymbol{\varepsilon}^p$ [24, 27].

$$\varepsilon = \varepsilon^e + \varepsilon^p \tag{1}$$

where bold-face symbols are used for variables of tensorial characteristics, and the plastic strain tensor $\boldsymbol{\varepsilon}^p$ represents all the irreversible deformations of the workpiece.

According to the fundamental concepts of the CDM, micro cracks and voids appear within the material under loading before the macro fracture of the workpiece. These micro damages could lead to the reduction of the material properties such as the moduli and strengths. In order to quantify the performance degradation, a damage factor d is applied, and an example is given here to explain its function. As shown in Fig. 1, when the material is subjected to the uniaxial load F, the induced micro damage (black dots in Fig. 1a) could result in the reduction of the effective load bearing area, from the cross-sectional area A of the original specimen, to the reduced effective load bearing area $\tilde{A}$ (see Fig. 1b) [28]. The area $\tilde{A}$ reads:

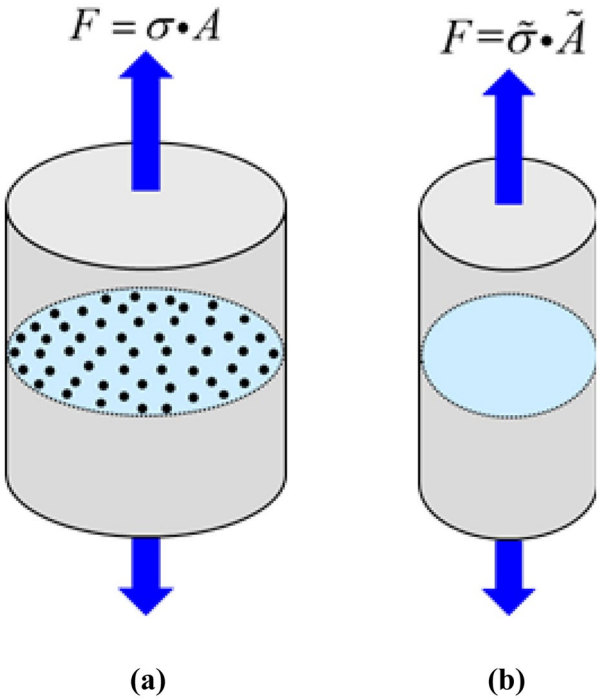

Fig. 1 Change of the effective load bearing area due to micro damage: (**a**) cross-sectional area with micro damage; (**b**) reduced effective load bearing area [28, 29]

$$\tilde{A} = (1 - d)A \tag{2}$$

In this case, the transmitted stress in the damaged material $\boldsymbol{\sigma}$ (Fig. 1a) could be derived [28, 29]:

$$\sigma = \frac{F}{A} = \frac{\tilde{\sigma} \cdot \tilde{A}}{A} = (1 - d)\tilde{\sigma} \tag{3}$$

where $\boldsymbol{\sigma}$ is the Cauchy nominal stress tensor, $\tilde{\boldsymbol{\sigma}}$ denotes the effective stress tensor and represents the stress in the assumed undamaged material (Fig. 1b).

Then, the stress–strain relationships for undamaged and damaged materials are presented as [21, 22]:

$$\begin{aligned} \tilde{\sigma} &= C_0 : \varepsilon^e \\ \sigma &= C_D : \varepsilon^e \end{aligned} \tag{4}$$

In which, symbol (:) denotes the inner product of two tensors with double contraction. $\boldsymbol{C_0}$ and $\boldsymbol{C_D}$ are the stiffness matrices for the undamaged and damaged unidirectional CFRTPs, respectively, and they are expressed by Eqs. 5–8 [30].

$$\boldsymbol{C_0} = \begin{bmatrix} C_{11} & C_{12} & C_{13} & & & \\ & C_{22} & C_{23} & & & \\ & & C_{33} & & & \\ & \text{Symmetric} & & G_{12} & & \\ & & & & G_{13} & \\ & & & & & G_{23} \end{bmatrix} \tag{5}$$

$$\begin{cases} C_{11} = \left(1 - \nu_{23}\nu_{32}\right)E_{11}/\Delta \\ C_{22} = \left(1 - \nu_{13}\nu_{31}\right)E_{22}/\Delta \\ C_{33} = \left(1 - \nu_{21}\nu_{13}\right)E_{33}/\Delta \\ C_{12} = \left(\nu_{12} + \nu_{32}\nu_{13}\right)E_{22}/\Delta \\ C_{13} = \left(\nu_{13} + \nu_{12}\nu_{23}\right)E_{33}/\Delta \\ C_{23} = \left(\nu_{23} + \nu_{21}\nu_{13}\right)E_{33}/\Delta \\ \Delta = 1 - \nu_{12}\nu_{21} - \nu_{23}\nu_{32} - \nu_{13}\nu_{31} - 2\nu_{21}\nu_{32}\nu_{13} \end{cases} \tag{6}$$

$$\boldsymbol{C_D} = \begin{bmatrix} C_{D11} & C_{D12} & C_{D13} & & & \\ & C_{D22} & C_{D23} & & & \\ & & C_{D33} & & & \\ & \textit{Symmetric} & & G_{D12} & & \\ & & & & G_{D13} & \\ & & & & & G_{D23} \end{bmatrix} \tag{7}$$

$$\begin{cases} C_{D11} = (1 - d_1)E_{11}(1 - (1 - d_2)(1 - d_3)\nu_{23}\nu_{32})/\Delta \\ C_{D22} = (1 - d_2)E_{22}(1 - (1 - d_1)(1 - d_3)\nu_{13}\nu_{31})/\Delta \\ C_{D33} = (1 - d_3)E_{33}(1 - (1 - d_1)(1 - d_2)\nu_{12}\nu_{21})/\Delta \\ C_{D12} = (1 - d_1)(1 - d_2)E_{11}(\nu_{21} + (1 - d_3)\nu_{23}\nu_{31})/\Delta \\ C_{D13} = (1 - d_1)(1 - d_3)E_{11}(\nu_{31} + (1 - d_2)\nu_{21}\nu_{32})/\Delta \\ C_{D23} = (1 - d_2)(1 - d_3)E_{22}(\nu_{32} + (1 - d_1)\nu_{12}\nu_{31})/\Delta \\ G_{D12} = (1 - d_{12})G_{12} \\ G_{D13} = (1 - d_{13})G_{13} \\ G_{D23} = (1 - d_{23})G_{23} \\ \Delta = 1 - (1 - d_1)(1 - d_2)\nu_{12}(\nu_{21} + (1 - d_3)\nu_{23}\nu_{31}) \\ \quad -\nu_{32}\nu_{23} + d_2\nu_{23}\nu_{32} + d_3\nu_{23}\nu_{32} - d_2d_3\nu_{23}\nu_{32} \\ \quad -(1 - d_1)(1 - d_3)\nu_{13}(\nu_{31} + (1 - d_2)\nu_{21}\nu_{32}) \end{cases} \tag{8}$$

where the subscript 1, 2 and 3 represent the longitudinal direction, transverse direction and through-thickness direction of the unidirectional composite laminates, respectively. E_{ii}, G_{ij}, and ν_{ij}, (i, j = 1, 2 and 3) are respectively the original Young's moduli, shear moduli and Poisson's ratios of an undamaged ply. d_i and d_{ij} (i, j = 1, 2 and 3) are the damage factors in the longitudinal, transverse, and through-thickness directions and the three shear damage factors, respectively.

2.1.2 Plastic Model

For the damaged composites, the internal stress generated by the external load is borne by the undamaged part of the material. Therefore, it could be supposed that the plastic

deformation occurs in the effective area of the damaged material, and the plastic flow and hardening laws are related to the effective stress. In this case, the plastic yield function expressed in terms of effective stress tensor $\tilde{\boldsymbol{\sigma}}$, equivalent plastic strain $\tilde{\varepsilon}^p$ are adopted in this research [21, 31]:

$$F(\tilde{\sigma}, \tilde{\varepsilon}^p) = f^p(\tilde{\sigma}) - \sigma_y(\tilde{\varepsilon}^p) \tag{9}$$

where f^p is the plastic potential, σ_y is the current yield stress which represents the hardening law. In this equation, the yield function F is less than or equal to zero if no plasticity occurs; while when F is greater than zero, the material has already yielded. Note that the equivalent plastic strain $\tilde{\varepsilon}^p$ is a scalar, and it never decreases because of the irreversibility of the plastic deformation.

The current work analysed the stress–strain relationships of the CFRTPs in the longitudinal, transverse and through-thickness directions and the three shear planes to define the plastic potential function f^p, as shown in Fig. 2. It is assumed that the material behaviour in the longitudinal direction is elastic, and there is no plastic flow in this direction (see Fig. 2a). Thus, the plastic potential function is determined to be independent on the longitudinal effective stress $\tilde{\sigma}_{11}$ [31, 32]:

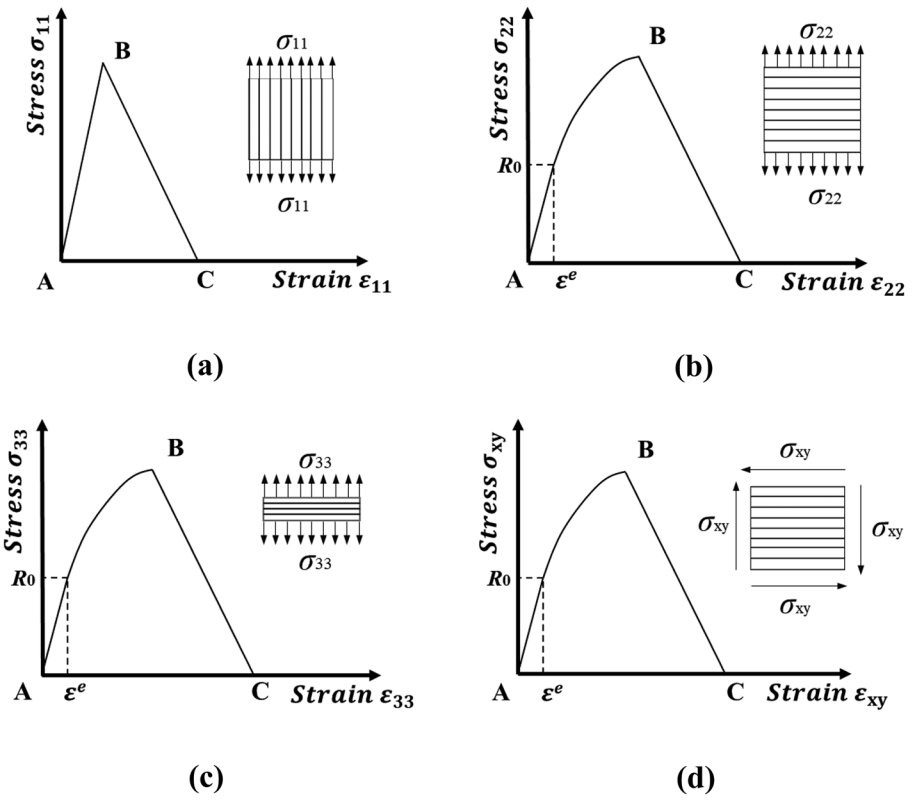

Fig. 2 Stress–strain relationships of the CFRTPs: (**a**) longitudinal direction; (**b**) transverse direction; (**c**) through-thickness direction; (**d**) three shear planes

$$f^p = \sqrt{\tilde{\sigma}_{12}^2 + \tilde{\sigma}_{23}^2 + \tilde{\sigma}_{13}^2 + c^2\left[\tilde{\sigma}_{22}^2 + \tilde{\sigma}_{33}^2\right]} \tag{10}$$

where $\tilde{\sigma}_{22}$ and $\tilde{\sigma}_{33}$ are the effective stresses in the transverse and through-thickness directions, respectively. $\tilde{\sigma}_{12}$,

$\tilde{\sigma}_{13}$ and $\tilde{\sigma}_{23}$ denote the effective stresses in the three corresponding shear planes. c is a coupling parameter which describes the level of plastic deformation developed under normal loads compared to the shear loads.

Due to its extensive application, the isotropic hardening law expressed in terms of equivalent plastic strain $\tilde{\varepsilon}^p$ is adopted [31, 32]:

$$\sigma_y(\tilde{\varepsilon}^p) = R_0 + \beta(\tilde{\varepsilon}^p)^\mu \tag{11}$$

In which, R_0 is the initial yield stress (R_0), β and μ are the hardening parameters.

On the basis of the plastic flow rule, the increment of the plastic strain tensor reads [27]:

$$d\varepsilon^p = \Delta\lambda \frac{\partial F}{\partial \tilde{\sigma}} \tag{12}$$

where $\Delta\lambda$ is a nonnegative plastic consistency parameter (plastic multiplier). Then, the equivalent plastic strain increment could be derived by substituting Eqs. 9–12 into the equivalence principle of the plastic work increment $dW^p = f^p(\tilde{\sigma}) \cdot d\tilde{\varepsilon}^p = \tilde{\sigma} : d\varepsilon^p$ [24, 32]:

$$d\tilde{\varepsilon}^p = \Delta\lambda \tag{13}$$

2.1.3 Numerical Implementation for Plasticity

The numerical simulation of the above nonlinear and irreversible material model is an incremental process, and the loading history is discretised into a series of time intervals $\left[t_n, t_{n+1}\right], n \in \{0, 1, 2, 3, \cdots\}$. In this case, by referring to the stress–strain relationship in Eqs. 3 and 4, the plastic yield function in Eq. 9, the hardening law in Eq. 11 and the plastic flow rule in Eq. 12, the implicit integration algorithm could be formulated as Eq. 14 [24] using the radial returns predictor algorithm based on the backward Euler integration procedure. Where $\tilde{\sigma}_{n+1}^{trial}$ is the trial stress tensor; the subscript n and $n+1$ represent the variables in the previous and current increment step, respectively.

$$\begin{aligned}
&\varepsilon_{n+1} = \varepsilon_n + \Delta\varepsilon_{n+1} \\
&\tilde{\sigma}_{n+1}^{trial} = \tilde{\sigma}_n + C_0 : \Delta\varepsilon_{n+1} \\
&\Delta\varepsilon_{n+1}^p = \Delta\lambda_{n+1} \frac{\partial F_{n+1}}{\partial \tilde{\sigma}_{n+1}} \\
&\tilde{\varepsilon}_{n+1}^p = \tilde{\varepsilon}_n^p + \Delta\tilde{\varepsilon}_{n+1}^p \\
&\varepsilon_{n+1}^p = \varepsilon_n^p + \Delta\varepsilon_{n+1}^p \\
&\tilde{\sigma}_{n+1} = \tilde{\sigma}_{n+1}^{trial} - \Delta\tilde{\sigma}_{n+1} = C_0 : \left(\varepsilon_{n+1} - \varepsilon_{n+1}^p\right) \\
&F_{n+1}\left(\tilde{\sigma}_{n+1}, \sigma_y\left(\tilde{\varepsilon}_{n+1}^p\right)\right) \le TOL
\end{aligned} \tag{14}$$

Driven by the strain increment $\Delta\varepsilon_{n+1}$ in the current step, plastic variables $\Delta\varepsilon_{n+1}^p, \Delta\tilde{\varepsilon}_{n+1}^p$ could be determined according to Eq. 14. Then, combined with the variables $\varepsilon_n, \varepsilon_n^p, \tilde{\varepsilon}_n^p, \tilde{\sigma}_n$

in the previous increment, the variables $\varepsilon_{n+1}, \varepsilon^{p}_{n+1}, \tilde{\varepsilon}^{p}_{n+1}, \tilde{\sigma}_{n+1}$ are updated. These stresses and state variables are stored and passed to the next increment. The solution of this discrete problem for the elastic–plastic material model could be explained in detail as follows. For a given load step, the increment is assumed to be elastically dominated at the beginning of this step and $\Delta\varepsilon^{p}_{n+1} = 0$, and the element of the workpiece has not yield. Under this circumstance, the total strain increment $\Delta\varepsilon_{n+1} = \Delta\varepsilon^{e}_{n+1}$, and the trial stress $\tilde{\sigma}^{trial}_{n+1}$ could be easily calculated utilising the elastic stiffness matrix. Then, $\tilde{\sigma}^{trial}_{n+1}$ is substituted in Eqs. 9 and 10, and to evaluate whether the current load step is in the elastic or plastic domain. If the obtained F_{n+1} is less than or equal to zero, no plasticity is occurring during the current increment indeed, and the procedure is processed to the next load step. Otherwise, plastic deformation has been produced and the plastic strain is determined by applying the iterative algorithm as described below. According to the plastic consistency condition, the stress and strain tensors on the yield surface should satisfy $F \equiv 0$ and $dF = 0$, and this leads to compute the plastic strain [24]:

$$d\tilde{\varepsilon}^{p} = \frac{(\partial F/\partial\tilde{\sigma})C}{(\partial F/\partial\tilde{\sigma})^{T}C(\partial F/\partial\tilde{\sigma}) + \left(\partial\sigma_{y}/\partial\tilde{\varepsilon}^{p}\right)} d\varepsilon = a \cdot d\varepsilon \tag{15}$$

Once the plastic yield function is greater than zero, the stress tensor should be returned to the yield surface. To this aim, Eq. 15 is implemented in Eq. 14 to calculate the plastic strain tensor and the equivalent plastic strain using the normal of the last yield surface, and then the trial stress is corrected. This new trial stress is substituted in Eqs. 9 and 10 again to compute the new F_{n+1}, and the above process is conducted repeatedly to ensure that the final F_{n+1} is less than *TOL*. Where *TOL* represents the chosen error tolerance and equals to 1×10^{-5} in this research. The whole iterative correction procedure based on the radial returns predictor algorithm is illustrated in Fig. 3. It should be noted that the total strain ε remains constant during the iteration, and the undamaged material stiffness tensor is used in both the trial stress and plastic corrector calculations.

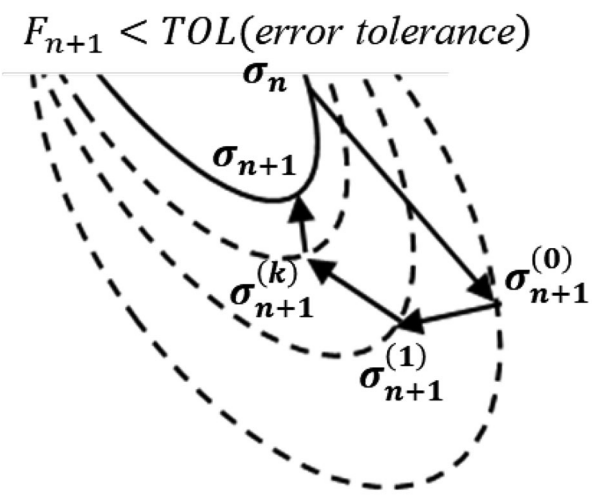

Fig. 3 Schematic diagram of the iterative correction procedure

From the above procedure, the plastic strain tensor $\boldsymbol{\varepsilon}_{n+1}^{p}$ is acquired. The Cauchy stress tensor is updated as below [24]:

$$\sigma_{n+1} = C_D : \left(\varepsilon_{n+1} - \varepsilon_{n+1}^{p}\right) \tag{16}$$

This work utilizes the Abaqus/Explicit commercial software to simulate the CFRTP cutting, hence the procedure described in this section should be implemented into the FE

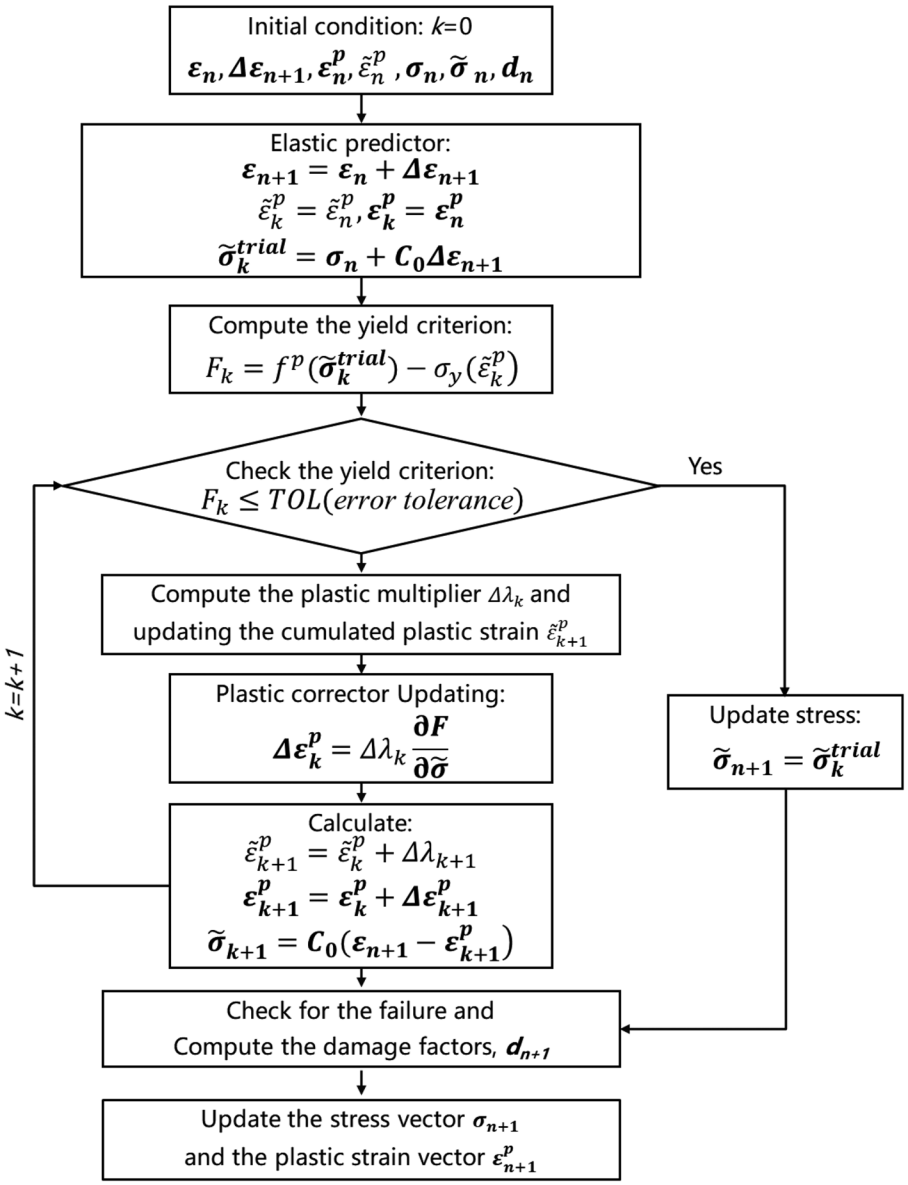

Fig. 4 Flow chart for the solution procedure of the constitutive model

software through the user-defined subroutine VUMAT. A flow chart is provided in Fig. 4 to make the procedure easy to understand.

2.1.4 Damage Initiation and Evolution Laws Based on the Strength

The fracture process of the CFRTPs under intensive loads is quite complex, and the various damage modes including fibre tensile failure, fibre compressive failure, matrix tensile failure and matrix compressive failure happen frequently. Previous studies [33, 34] have applied combined Hashin and Puck criteria for the simulation of low velocity impact testing, and the results indicated the successful prediction for the individual damages of composites with the good agreement with experimental measurements. Therefore, this paper cites the damage theories proposed by Hashin [35, 36] and Puck [37–39] too to simulate the damage initiation of the unidirectional CFRTPs during the cutting. Specifically, the Hashin criteria are selected to predict the fibre fracture and matrix tensile failure, and the matrix compressive failure is estimated based on the research of Puck:

Fibre tensile failure:

$$\sigma_{11} \geq 0 \rightarrow f_{ft} = \left(\frac{\sigma_{11}}{X_T}\right)^2 + \left(\frac{\tau_{12}}{S_{12}}\right)^2 + \left(\frac{\tau_{13}}{S_{13}}\right)^2; f_{ft} \geq 1 \tag{17}$$

Fibre compressive failure:

$$\sigma_{11} < 0 \rightarrow f_{fc} = \left(\frac{\sigma_{11}}{X_C}\right)^2; f_{fc} \geq 1 \tag{18}$$

Matrix tensile failure:

$$\sigma_{22} \geq 0 \rightarrow f_{mt} = \left(\frac{\sigma_{22}}{Y_T}\right)^2 + \left(\frac{\tau_{12}}{S_{12}}\right)^2 + \left(\frac{\tau_{23}}{S_{23}}\right)^2; f_{mt} \geq 1 \tag{19}$$

Matrix compressive failure:

$$\sigma_{22} < 0 \rightarrow f_{mc} = \left(\frac{\tau_T}{S_T - \mu_T \sigma_n}\right)^2 + \left(\frac{\tau_L}{S_L - \mu_L \sigma_n}\right)^2; f_{mc} \geq 1 \tag{20}$$

where f is the failure initiation index. The subscripts f and m express the fibre and matrix failure, respectively; the subscripts t and c symbolise tensile and compressive failure, respectively. X_T and X_C denote the tensile and compressive strengths of the unidirectional CFRTPs in the longitudinal direction, while Y_T is the tensile strength in the transverse direction. S_{ij} (i, j = 1, 2 and 3) is the corresponding shear strength.

The unidirectional CFRTPs are usually fractured along a plane with an angle to the through-thickness direction under compression loading in the transverse direction, and the angle is defined to be θ in this work as shown in Fig. 5. σ_n, τ_T and τ_L in Eq. 20 are the traction stress components in the normal, transverse and longitudinal directions on the fracture plane, respectively. They are obtained from the components of the stress tensor and the fracture plane angle θ [38, 39]:

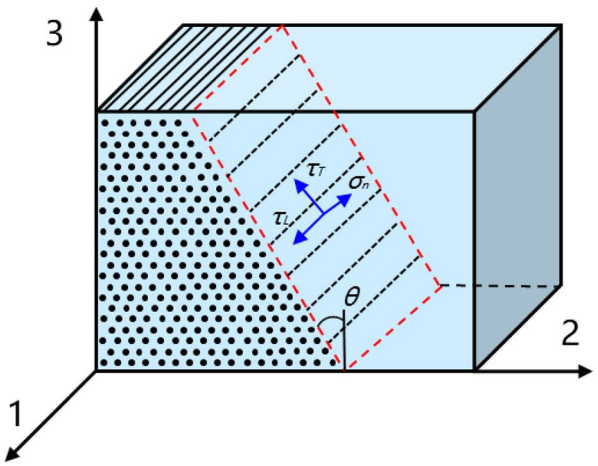

Fig. 5 Fracture plane of unidirectional CFRTPs under transverse compression loading

$$\begin{aligned}\sigma_n &= \sigma_{22}\cos^2\theta + \sigma_{33}\sin^2\theta + 2\tau_{23}\sin\theta\cos\theta \\ \tau_T &= (\sigma_{33} - \sigma_{22})\sin\theta\cos\theta + \tau_{23}(\cos^2\theta - \sin^2\theta) \\ \tau_L &= \tau_{31}\sin\theta + \tau_{21}\cos\theta\end{aligned} \tag{21}$$

$S_T = Y_C/2\tan(\theta)$ and $S_L = S_{12}$ are both the shear strengths in the fracture plane. Y_C is the compressive strength in the transverse direction. μ_T and μ_L are friction coefficients, and they are defined as $\mu_T = -1/\tan(2\theta)$, $\mu_L = \mu_T S_L/S_T$ [40].

After the damage initiation, the material stiffness of CFRTPs degrades with the irreversible evolution of damage under the external cutting load. In this work, linear damage evolution laws are applied for the four failure modes, and the stiffness is gradually reduced under the control of the damage factor d. The damage factor is calculated based on the strain variable ε at each time step, and the damage onset strain ε^0 and complete failure strain ε^f, as shown by Eq. 22 [6]. It has the value 0 at onset of failure and value 1 at final failure.

$$d = \frac{\varepsilon^f}{\varepsilon^f - \varepsilon^0}\left(1 - \frac{\varepsilon^0}{\varepsilon}\right) \tag{22}$$

To be specific, the damage factors for fibre (d_{1E}) failure and matrix (d_{2E}) tensile failure modes are:

$$\begin{cases} f_{ft} \geq 1 \rightarrow d_{1E} = \frac{\varepsilon^f_{ft}}{\varepsilon^f_{ft} - \varepsilon^0_{ft}}\left(1 - \frac{\varepsilon^0_{ft}}{\varepsilon_{ft}}\right) \\ f_{fc} \geq 1 \rightarrow d_{1E} = \frac{\varepsilon^f_{fc}}{\varepsilon^f_{fc} - \varepsilon^0_{fc}}\left(1 - \frac{\varepsilon^0_{fc}}{\varepsilon_{fc}}\right) \\ f_{mt} \geq 1 \rightarrow d_{2E} = \frac{\varepsilon^f_{mt}}{\varepsilon^f_{mt} - \varepsilon^0_{mt}}\left(1 - \frac{\varepsilon^0_{mt}}{\varepsilon_{mt}}\right) \end{cases} \tag{23}$$

where the damage onset strains (ε^0_{ft}, ε^0_{fc} and ε^0_{mt}) are determined when the corresponding failure criterion is satisfied, and the final failure strains (ε^f_{ft}, ε^f_{fc} and ε^f_{mt}) are given by Eq. 24 [30]:

$$\begin{cases} \varepsilon_{ft}^{f} = \frac{2G_{fC}^{T}}{X_T L^c} \\ \varepsilon_{fc}^{f} = \frac{2G_{fC}^{C}}{X_C L^c} \\ \varepsilon_{mt}^{f} = \frac{2G_{mC}^{T}}{Y_T L^c} \end{cases} \tag{24}$$

In which, G_{fC}^{T}, G_{fC}^{C} and G_{mC}^{T} denote the fracture toughness associated with these three generic failure modes, respectively. L^c is the characteristic length of the elements, and it is introduced to reduce the mesh dependency of the simulation results.

While for the compressive failure in the transverse direction, the damage factor is defined by the strain acting on the fracture plane:

$$f_{mc} \geq 1 \rightarrow d_{2E} = \frac{\varepsilon_{matc}^{f}}{\varepsilon_{matc}^{f} - \varepsilon_{matc}^{0}} \left(1 - \frac{\varepsilon_{matc}^{0}}{\varepsilon_{matc}} \right) \tag{25}$$

where $\varepsilon_{matc} = \sqrt{\langle \varepsilon_n \rangle^2 + \gamma_T^2 + \gamma_L^2}$ [30, 41]. The symbol $\langle \bullet \rangle$ indicates that, for any real number x, $\langle x \rangle = (x + |x|)/2$. The strain components in the normal, transverse and longitudinal directions on the fracture plane read:

$$\begin{aligned} \varepsilon_n &= \varepsilon_{22} \cos^2 \theta + \varepsilon_{33} \sin^2 \theta + \gamma_{23} \sin \theta \cos \theta \\ \gamma_T &= 2\left(\varepsilon_{33} - \varepsilon_{22}\right) \sin \theta \cos \theta + \gamma_{23} \left(\cos^2 \theta - \sin^2 \theta \right) \\ \gamma_L &= \gamma_{31} \sin \theta + \gamma_{21} \cos \theta \end{aligned} \tag{26}$$

The onset strain ε_{matc}^{0} is obtained from the value of ε_{matc} at the onset of matrix compressive failure. The expression for final failure strain ε_{matc}^{f} is [30, 41]:

$$\varepsilon_{matc}^{f} = \frac{2G_{matC}^{C}}{\sigma_{matc}^{0} L^c} \tag{27}$$

The determination of the onset stress σ_{matc}^{0} is similar to that of the ε_{matc}^{0}, i.e. [30, 41]:

$$\sigma_{matc}^{0} = \sigma_{matc}|_{f_{mc}=1} = \sqrt{\langle \sigma_n \rangle^2 + \tau_T^2 + \tau_L^2}|_{f_{mc}=1} \tag{28}$$

G_{matC}^{C} denotes the fracture toughness, and it is formulated as [30, 41]:

$$G_{matC}^{C} = G_{IC} \left(\frac{\sigma_n}{\sigma_{matc}^{0}} \right)^2 + G_{IIC} \left(\frac{\tau_T}{\sigma_{matc}^{0}} \right)^2 + G_{IIC} \left(\frac{\tau_L}{\sigma_{matc}^{0}} \right)^2 \tag{29}$$

In which, G_{IC} and G_{IIC} are the fracture toughness for the mode I and II fractures, respectively.

2.1.5 Damage Initiation and Evolution Laws Based on the Strain Energy Density

The strain energy density of the damaged CFRTP ply in the 3D configuration is defined as [30]:

$$E_D = \frac{1}{2}\left(\begin{array}{c} \left(\frac{\sigma_{11}^2}{E_{11}(1-d_1)}\right) + \left(\frac{\sigma_{22}^2}{E_{22}(1-d_2)}\right) + \left(\frac{\sigma_{33}^2}{E_{33}}\right) - 2\left(\frac{\sigma_{11}\sigma_{22}\nu_{12}}{E_{11}}\right) \\ -2\left(\frac{\sigma_{11}\sigma_{33}\nu_{13}}{E_{11}}\right) - 2\left(\frac{\sigma_{22}\sigma_{33}\nu_{23}}{E_{22}}\right) + \left(\frac{\tau_{12}^2}{G_{12}(1-d_{12})}\right) + \left(\frac{\tau_{13}^2}{G_{13}}\right) + \left(\frac{\tau_{23}^2}{G_{23}}\right) \end{array} \right) \tag{30}$$

Let us consider the irreversible energy dissipation, the thermodynamic force vectors conjugated to damage in the transverse direction and 1–2 plane could be derived [24, 26]:

$$\begin{aligned} Y_2 &= \frac{\partial E_D}{\partial d_2} \\ Y_{12} &= \frac{\partial E_D}{\partial d_{12}} \end{aligned} \tag{31}$$

The initiation of damage and its evolution [26] are governed by the square root of a linear combination of the two damage variables Y_2 and Y_{12}, as shown in Eq. 32 [26, 42]:

$$\begin{aligned} &\underline{Y}(t) = \max_{s \le t}\left(\sqrt{Y_{12}(s) + bY_2(s)}\right) \\ &\Rightarrow \begin{cases} \underline{Y}(t) > Y_{2_0} \rightarrow d_{2G} = \frac{\underline{Y}(t) - Y_{2_0}}{Y_{2_c}} \\ \underline{Y}(t) > Y_{12_0} \rightarrow d_{12G} = \frac{\underline{Y}(t) - Y_{12_0}}{Y_{12_c}} \end{cases} \end{aligned} \tag{32}$$

where $\underline{Y}$ is defined to be the maximum value of it from any previous time, s, up to the current time, t, to avoid the healing of damage. b is the shear-transverse damage coupling factor. Y_{2_0} and Y_{12_0} are the initial transverse and shear threshold values, respectively, while Y_{2_c} and Y_{12_c} are the slope of $\underline{Y}(t)$ versus respectively d_{2G} and d_{12G}.

The final damage factors d_i and d_{ij} (i, j = 1, 2 and 3) for each increment step are calculated by combining the damage initiation and evolution laws based on both the strength and strain energy density:

$$\begin{aligned} d_1 &= d_{1E} \\ d_2 &= \max(d_{2E}, d_{2G}) \\ d_{12} &= \max(d_{2E}, d_{12G}) \\ d_3 &= d_{13} = d_{23} = d_{2E} \end{aligned} \tag{33}$$

The damage initiation and evolution laws are defined in the VUMAT together with the material constitutive model. The material properties of the CFRTPs are obtained by consulting manufacturers and referring to Reference [21, 23, 43], and are listed in Table 1.

2.2 Geometric Model and Boundary Conditions

Figure 6 illustrates the geometric model for the simulation of CFRTP machining. By comparing the different machining approaches (e.g. orthogonal cutting, drilling and milling), it is clear that the tool-workpiece interactions are complex during the drilling or milling, especially in the processing of angle ply composite laminates. Several factors such as fibre orientation and cutter structures are all introduced in one trial simultaneously, and thus their influences on the damage extent are hard to be distinguished. Therefore, the orthogonal cutting of unidirectional CFRTPs is conducted in this investigation.

The tool is defined as an analytical rigid body for a higher computational efficiency. The workpiece is set to be a deformable solid with a length of 1.2 mm, a height of 1 mm and a width of 0.1 mm to save the calculation time. To further improve the computational

Table 1 Material properties of the CFRTPs [21, 23, 43]

Properties	Value	Properties	Value	Properties	Value
E_{11} (GPa)	127	μ	0.38	$Y_{12_0}(\sqrt{MPa})$	48
$E_{22}=E_{33}$ (GPa)	10.3	R_0	21.59	$Y_{2_0}(\sqrt{MPa})$	100
$G_{12}=G_{13}$ (GPa)	5.7	θ (°)	53	$Y_{12_c}(\sqrt{MPa})$	3000
G_{23} (GPa)	3.2	X_T (MPa)	2070	$Y_{2_c}(\sqrt{MPa})$	3100
$\nu_{12}=\nu_{13}$	0.3	X_C (MPa)	1360	G_{fC}^{T}(kJ/m^2)	218
ν_{23}	0.3	Y_T (MPa)	102	G_{fC}^{C}(kJ/m^2)	104
c	0.73	Y_C (MPa)	276	$G_{mC}^{T}=G_{IC}$(kJ/m^2)	1.7
b	0.53	$S_{12}=S_{13}$ (MPa)	186	G_{IIC}(kJ/m^2)	2.0
β	558	S_{23} (MPa)	186	ρ (g/cm^3)	1.58

efficiency with a guaranteed accuracy, the meshes in the cutting area of the workpiece are refined with the size of 0.01 mm and 0.04 mm coarse elements are set in the rest area. The workpiece adopts 8-node linear brick elements with reduced integration (C3D8R), and the enhanced hourglass control approach is applied to minimise the potential risk from hourglass issue.

The CFRTPs are fixed by constraining all degrees of freedom of the nodes at the bottom and left sides of the workpiece. The tool is only allowed to move along the X axis in Fig. 6 to cut the composites with a constant cutting speed of 10 mm/s. The cutting of unidirectional CFRTPs with the four typical fibre orientations (i.e. 0°, 45°, 90° and 135°) is simulated first to validate the numerical model. In this part of our study, a 25° tool rake angle, a 5° clearance angle, and a 10 μm tool edge radius are selected, and the cutting depth is 50 μm. And then, a variable parameter study of subsurface damage and cutting

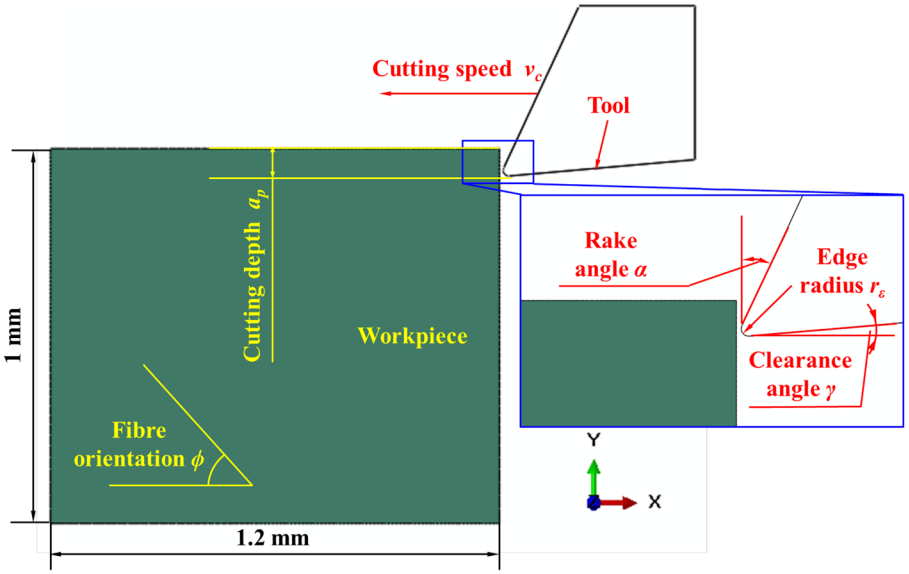

Fig. 6 Geometric model for the simulation of CFRTP orthogonal cutting

force changes during unidirectional cutting of CFRTP is carried out. The numerical points of the fibre orientation selected in our simulation study are similar to those in Reference [44]. So, the workpieces with the 30°, 60°, 120° and 150° fibres laid up are involved in the cutting prediction to further evaluate the change of the subsurface damage. The selections of cutting speed, cutting depth, tool clearance angle and tool edge radius are mainly based on references [14, 24, 44–47]. References [47, 48], and [49] are referenced in our research when selecting the rake angles of the tool, and the rake angle values are determined to be -15°, 0°, 15°, and 25°, respectively. The processing conditions are detailed in Table 2. The surface to surface kinematic contact algorithm is used to describe the dynamic interactions between the tool and workpiece. Wherein, the normal behaviour along the contact surface is defined to be hard contact, while the Coulomb friction algorithm is utilised to characterise the tangential behaviour. The friction coefficient is set as 0.5.

3 Experimental Setups

Orthogonal cutting experiments on the unidirectional CFRTPs are conducted in this research to validate the elastic–plastic damage model and the simulation of the CFRTP cutting. The experimental setup is shown in Fig. 7. The composite cutting is performed by fixing the tool and moving the CFRTP part. The workpiece is constrained on a platform powered by the linear motor, and it can move in a straight line at a constant speed under the traction of the linear motor. The cutting tool is fastened on the platform to keep it still. Unidirectional CFRTP laminates used in the experiments are produced by Junhua PEEK Ltd and they are made from carbon fibre/PEEK prepregs through a process including loading into mold, heating up, holding pressure, cooling, and demolding, which are 4 mm in thickness and contain 20 layers. The volume fraction of carbon fibre in the laminates is 60%. These laminates are cut into small sheets with the dimension of 50 mm × 90 mm by a diamond wire saw machine to facilitate the clamping. Four kinds of workpieces are prepared to observe the composite machining under the fibre orientations of 0°, 45°, 90° and 135°. The turning tool is applied and it is made from cemented carbide. The tool cutting edge radius is about 10 μm, and a new tool is employed for each cut to avoid the effect of tool wear.

The KISTLER 9257B three-component dynamometer is clamped under the cutting tool to measure the cutting force. The 5080 amplifier, 5697A data acquisition and force record terminal are employed to transmit and collect the force signals. The original signals of cutting forces are acquired at a sampling frequency of 12 kHz, and they are visualised and analysed with the commercial software DynoWare. A PHOTRON SA5

Table 2 Tool geometric parameters and processing conditions [14, 24, 44–49]

Parameters	Value
Rake angle α(°)	-15, 0, 15, 25
Clearance angle γ(°)	5
Edge radius r_ε(μm)	10, 20, 30
Fibre orientation ϕ(°)	0, 30, 45, 60, 90, 120, 135, 150
Cutting depth a_p(μm)	50, 100, 150, 200
Cutting speed v_c(mm/s)	10

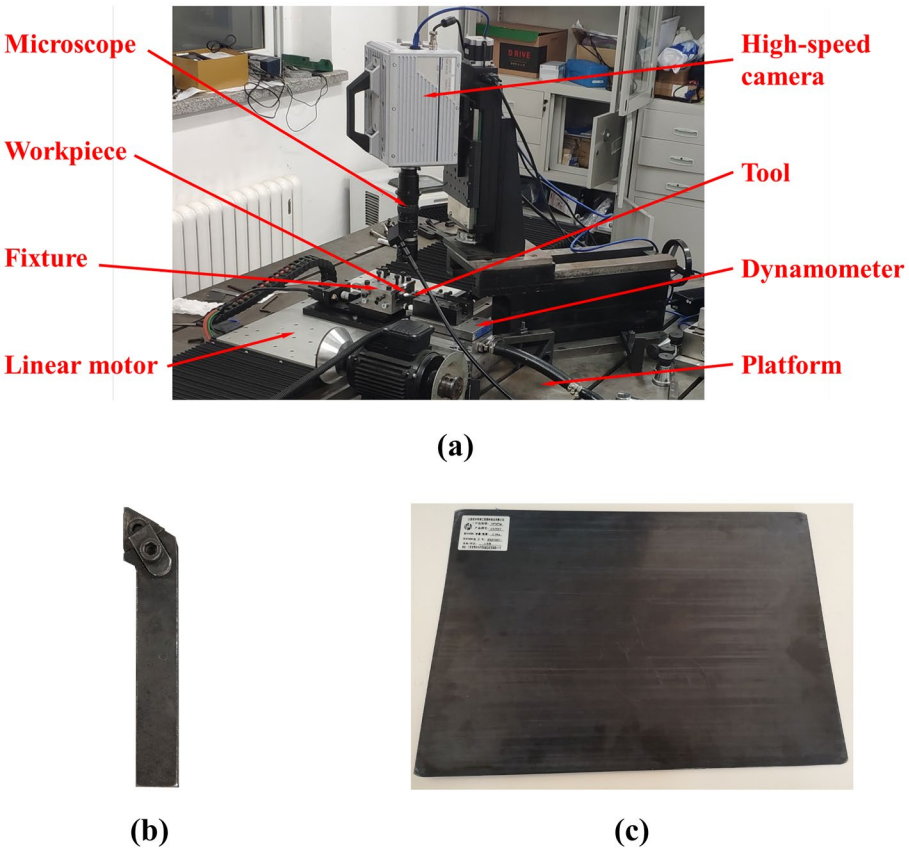

Fig. 7 Details of the orthogonal cutting experiment: (**a**) Experimental setups; (**b**) Tool; (**c**) Workpiece

high-speed camera with a VH-Z50L microscopic lens is selected to record the cutting process. It is found by testing the parameters of the high-speed camera that only fuzzy and dim video could be captured under high cutting speed, thus the CFRTP cutting is performed at a speed of 10 mm/s. Since a large cutting depth could induce the micro-chipping of the cutting edge and lead to the decrease of the result reliability, the 50 μm cutting depth is hence determined in these verification experiments. In addition, the experiments with the same processing conditions are repeated three times to reduce the error.

4 Simulation Validations

In this work, the simulated CFRTP cutting processes under the 0°, 45°, 90° and 135° fibre orientations are compared with the experimental observations to validate the elastic–plastic damage model and numerical modelling. The results including the material removal processes, chip morphologies and cutting forces are detailed as follows.

4.1 The Cutting Processes and Chip Morphologies of the CFRTPs

The simulated and experimentally recorded orthogonal cutting processes of the unidirectional CFRTPs are shown in Figs. 8–11. The von-Mises stresses are presented in the modelling results to demonstrate the process of material removal and the stress distribution during the machining process. In addition, the chips formed finally in the experiments are observed with an electron microscope to assist the analysis of the chip morphologies, as seen in Fig. 12.

Regarding to the cutting of CFRTPs laid up with 0° fibres only, the cutting direction is consistent with the fibre direction. High internal stresses are generated when the tool cutting edge contacts the workpiece (see Fig. 8a), and they are easy to lead the cracking of the matrix and the separating of the materials above the cutting plane with the rest of the workpiece. Then, the tool penetrates into the workpiece, and it raises the materials that are above the tool tip. Plastic deformations initiate in the cut material piece progressively with the advance of the tool, and the material is bent to the action direction of the rake face. With the further feed of the tool, the initial chips deform continuously, and C-shaped chips are generated under the action of the upper surface of the workpiece. The predicted chip formation process agrees well with the experimental observation, and the morphologies of the chips formed finally are consistent, as shown in Figs. 8 and 12a.

When cutting CFRTPs with 45° fibre orientation, high internal stresses are observed near the tool tip and along the fibre direction (see Fig. 9a). The cutting tool crushes the fibres and matrix at the cutting plane, and the materials above the cutting tool tip are forced to slide upward by the tool rake face. The cut material piece bends due to the persistent occurrence of the plastic deformation and it wraps together with the advance of the cutting tool. Subsequently, long and curly chips are formed when the machining finishes or some of the elements fail completely. The predicted material removal process and chip morphology are consistently recorded by the experiments using the high-speed camera system to successfully validate the accuracy of the elastic–plastic damage model developed in this research, as shown in Figs. 9 and 12b.

For the 90° fibre orientation, the cutting direction is perpendicular to the fibre direction. During the cutting process, the material in front of the cutting tool tip deforms under the

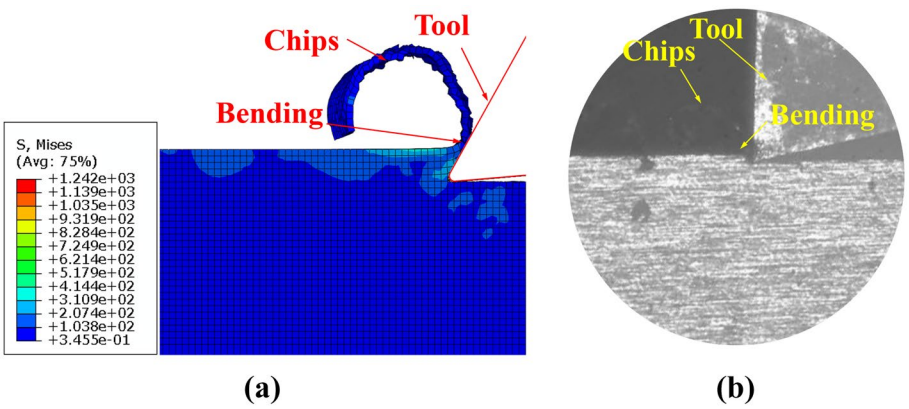

Fig. 8 Chip formation of the CFRTPs with 0° fibre orientation: (**a**) Simulation results; (**b**) Experimental observations

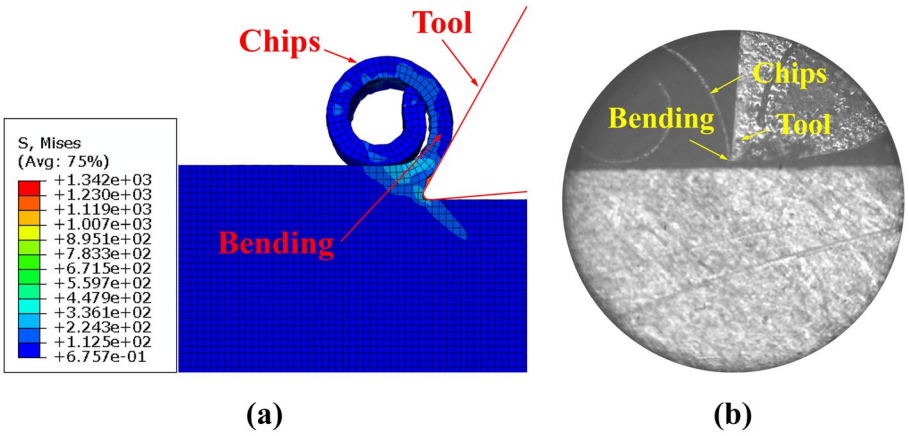

Fig. 9 Chip formation of the CFRTPs with 45° fibre orientation: (**a**) Simulation results; (**b**) Experimental observations

push of the tool (see Fig. 10a and c). In this case, multiple fibres and the adjacent matrix are bent and they fracture together at the cutting plane. Then, shear stresses are induced due to the upward squeezing of the tool cutting edge and they act onto the matrix between

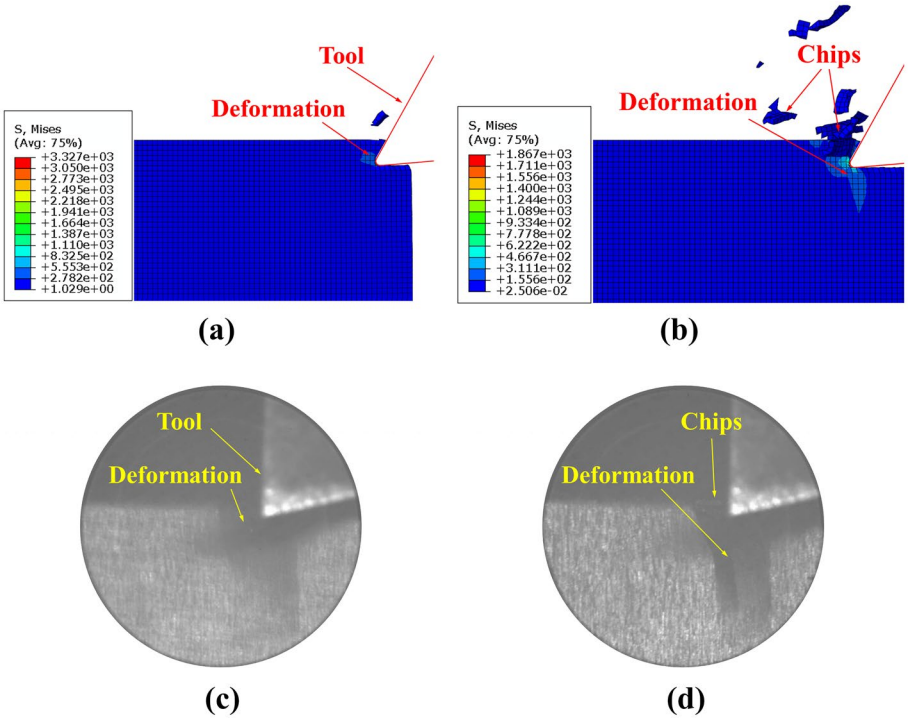

Fig. 10 Chip formation of the CFRTPs with 90° fibre orientation: (**a**) and (**b**) Simulation results; (**c**) and (**d**) Experimental observations

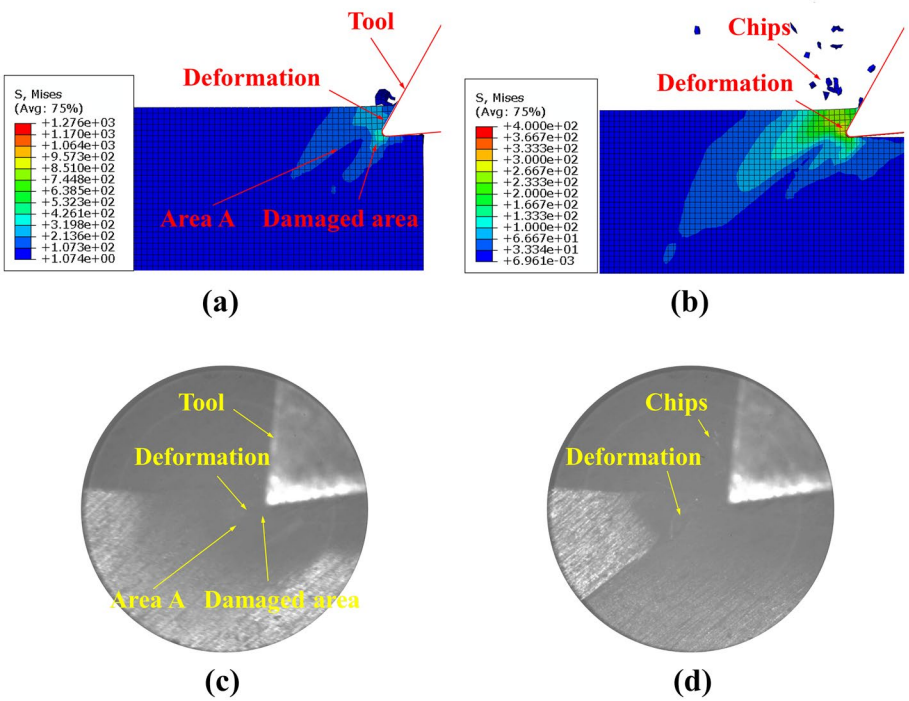

Fig. 11 Chip formation of the CFRTPs with 135° fibre orientation: (**a**) and (**b**) Simulation results; (**c**) and (**d**) Experimental observations

the fractured and non-damaged materials, and the failed fibres and matrix are removed and block-shaped chips are generated. It is clear that the simulation results acquired (see Fig. 10a and b) by the developed FE model are of high accuracy compared with the experimental measurements in Figs. 10c, d and 12c. In this process, the chip formation is mostly initiated by the bending fracture of the fibres, which is apparently different from the cutting process of the CFRTPs with 45° fibre orientation where the fibres are crushed by the tool.

The chip formation of the CFRTPs with 135° fibre orientation is shown in Fig. 11. Both the simulation and experimental results indicate that the push action of the tool tip leads to local failure of the material in the early stage of the machining process. Subsequently, the workpiece above the tool rake face deforms, and the damage is initiated near the tool cutting edge and it propagates downward along the fibre direction. The materials on the left side (Area A in Fig. 11a and c) of the damaged area start to be acted by the cutting tool, and the total amount of the material being cut increases. Since the tool rake angle is smaller than the Angle ϕ-90° (fibre orientation subtract 90°), a great squeezing effect is applied by the tool rake face rather than the tool tip on the fibres being cut. As the tool further feeds, the material contacting the tool rake face is bent to a critical state, and it fails and forms fragment-like chips (see Figs. 11b, d and 12d). The simulation results show a good agreement with the experimental measurements. Moreover, although the fibre bending occurs in both this cutting process and the cutting of CFRTPs with 90° fibre orientation, the chip morphologies of them are different. As mentioned above, for the 135° fibre orientation, the action of the cutting tool rake face is stronger than the cutting of the tool tip on the fibres.

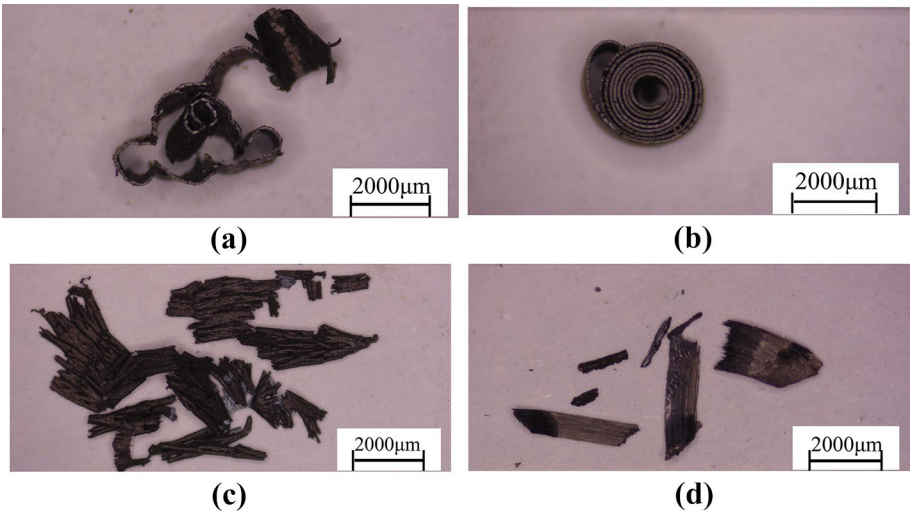

Fig. 12 Chip morphologies in the cutting of unidirectional CFRTPs: (**a**) 0° fibre orientation; (**b**) 45° fibre orientation; (**c**) 90° fibre orientation; (**d**) 135° fibre orientation

Under this circumstance, the fibres are not easy to break on the processing plane like that in the cutting of CFRTPs with 90° fibre orientation. While the tool rake face squeezes the material on the upper surface of the workpiece and fragment-like chips are generated.

To sum up, the predicted material removal and chip formation processes using the elastic–plastic damage model agree well with the experimental observations for the various composite layups. Furthermore, the chip morphologies in the simulation results are highly consistent with those in the experiments. Therefore, it could be concluded that the proposed numerical model possesses the ability to effectively simulate the CFRTP cutting, and it is applicable for the damage assessment.

4.2 The Cutting Forces in the CFRTP Orthogonal Cutting

The curves of cutting force per unit width versus tool displacement at the four typical fibre orientations are shown in Fig. 13. Due to the removal of material during cutting, there are inevitably large fluctuations in simulations and experiments. In addition, considering the computational efficiency, the size of the finite element model is usually simplified in the cutting simulation study of FRPs [14, 24, 32, 44, 45, 47]. For the above reasons, we selected the force signals with a duration of about 0.02 s in the stable cutting stage at the four typical fibre orientations, respectively. To compare the experimental and simulation results, the cutting forces are converted into cutting forces per unit width, and the time axes of all force signals are offset and zeroed, and the force signals are filtered to remove the effect of noise. The simulation results are in good agreement with the experimental results.

In the cutting simulation study of FRPs, the average value of the cutting force in the steady cutting stage is usually used to compare the experimental and simulation results [14, 24, 32, 44, 45, 47]. Figure 14 illustrates the simulation and experimental cutting force per unit width for the CFRTPs with the four fibre orientations. It could be seen that the change of the numerical predicted cutting force per unit width with the fibre orientation

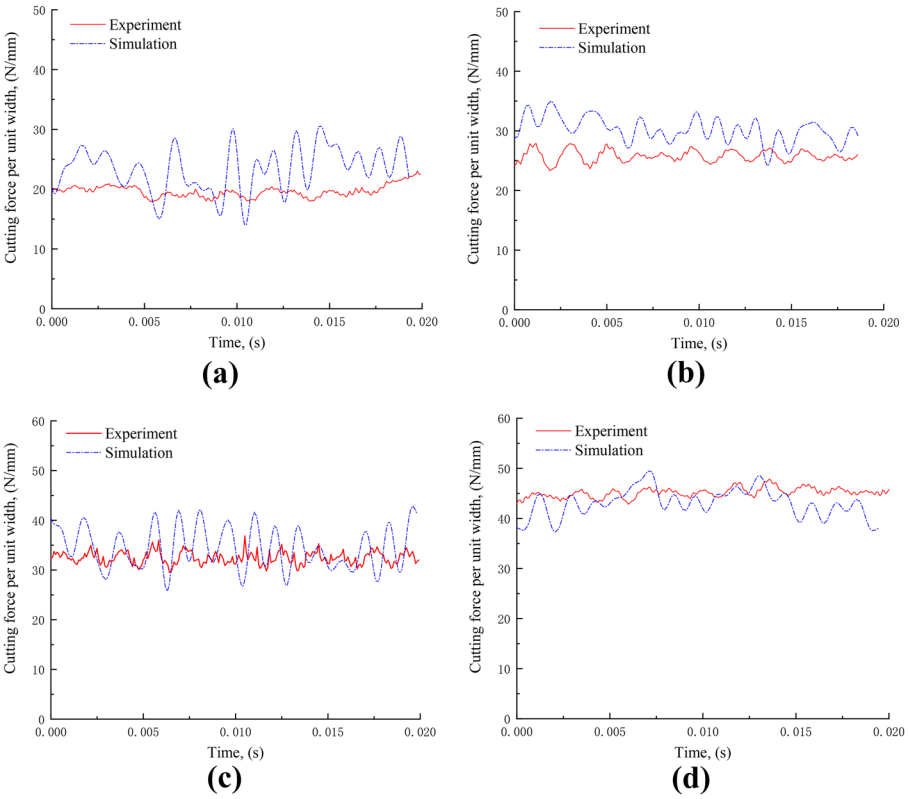

Fig. 13 The curves of cutting force per unit width versus tool displacement at the four typical fibre orientations: **a** 0° fibre orientation; **b** 45° fibre orientation; **c** 90° fibre orientation; **d** 135° fibre orientation

agrees well with that of the experimental outputs. The error between the simulation and experimental results is less than 20%. A higher cutting force per unit width is produced by a greater fibre orientation, and the maximum value obtained at 135° fibre orientation is about 45 N/mm. The reason for these outcomes could be explained by analysing the cutting processes of the CFRTPs with the four composite layups. As mentioned in Sect 4.1, the matrix cracking is the main failure mode of the material during the cutting of CFRTPs with 0° fibre orientation, and few fibres are cut in this case compared with that in the cutting of CFRTPs with the other three fibre orientations. Since the matrix strength is less than the fibre strength, the smallest cutting force is resulted in the 0° fibre orientation. With regard to the CFRTPs consisting of 45° fibres, the fibres have to be broken during the cutting process, and thus the cutting force is greater than that of the 0° fibre orientation. Whereas, in the cutting of CFRTPs with 45° fibre orientation, the fibres and matrix are crushed and the materials being cut are easy to slide upward and form the chips, which is different from the material removal process of the CFRTPs with 90° fibre layups whose fibres and matrix are fractured due to bending and the chips are generated under the upward squeezing of the tool cutting edge. Therefore, the cutting force of the CFRTPs with 90° fibre orientation is higher than that of the CFRTP laminates with 45° fibres only. In the last case of the 135° fibre orientation, the amount of the material being cut is larger than that in the cutting

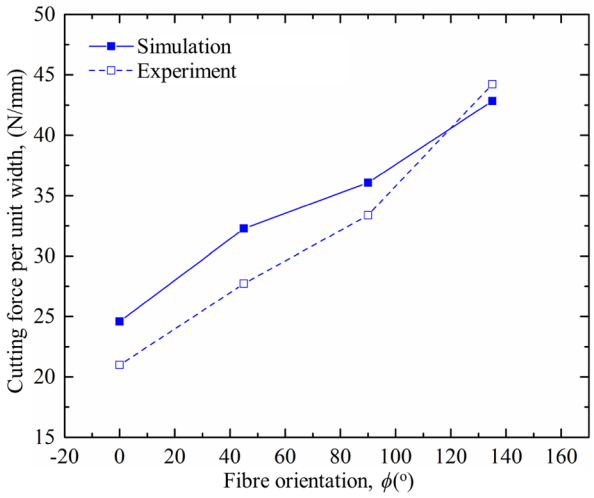

Fig. 14 Cutting force per unit width for the unidirectional CFRTPs with various fibre orientations

of CFRTPs with the other three fibre orientations although the same cutting depths are applied during these machining processes. In the meantime, the material removal is mostly attributed to the squeezing action of the tool rake face rather than the cutting of the tool cutting edge. Thus, the highest cutting force is generated in the cutting of the CFRTPs with 135° fibres laid up.

5 Discussions on the Subsurface Damage Depth Under Various Cutting Conditions

This section summarizes the parametric studies on the subsurface damage and cutting force conducted using the FE model for the CFRTP cutting. The influences of the fibre orientation, cutting tool rake angle, tool edge radius and cutting depth are described and discussed. Wherein, the distributions of the damage factor are illustrated to present the subsurface damage, and the area where the damage has been initiated ($d > 0$) is determined to be the subsurface damage zone to take the potential damage into account.

5.1 Influence of the Fibre Orientation

The predicted subsurface damage distributions in the cutting of CFRTPs with a tool of 25° rake angle and 10 μm cutting edge radius and under 50 μm cutting depth and various fibre orientations are shown in Fig. 15. Figure 16 is the variations in the cutting force per unit width and subsurface damage depths with the different fibre orientations. The cutting force and subsurface damage depth maintain an approximately growing trend with the increasing of the fibre orientation within the range of 0° to 135°, while a sharp decrease of them occurs at the 150° fibre orientation. The growth of the cutting force and subsurface damage at 0° to 135° fibre orientations can be explained as follows by referring to the interpretations for the results in Sect 4.2. As the increase of the fibre orientation from 0° to 135°, both the cracking direction of the workpiece and the cutting action of the tool

Fig. 15 Subsurface damage under various fibre orientations: **a** 0° fibre orientation; **b** 30° fibre orientation; **c** 45° fibre orientation; **d** 60° fibre orientation; **e** 90° fibre orientation; **f** 120° fibre orientation; **g** 135° fibre orientation; **h** 150° fibre orientation

vary obviously. The propagation direction of the crack and damage induced by the cutting process changes from leaving the workpiece upwards to invading the workpiece downwards, and the cutting action of the tool tip in the cutting plane is gradually replaced by the squeezing action of the tool rake face. The combination of these variations leads to the increase of the cutting force and subsurface damage. After the fibre orientation is greater than 135°, the cutting action of the tool on the CFRTPs is closer to that at the 0° fibre orientation, and thus the cutting force per unit width and subsurface damage depths become smaller. It should also be noticed that an unexpected drop of the cutting force happens at the 120° fibre orientation. When cutting CFRTPs with 120° fibres, the tool rake face is almost parallel to the fibre direction. The sliding and friction between the cutting tool and workpiece are enhanced while the cutting action applied on the workpiece is weaker, therefore, the cutting force is decreased.

5.2 Influence of the Tool Rake Angle

For the cutting of CFRTPs with 90° fibres laid up at a cutting depth of 50 μm using the tools with -15°, 0°, 15° and 25° rake angles and 10 μm cutting edge radius, the simulation results are shown in Fig. 17. The cutting force and subsurface damage induced by the 0° rake angle tool are greater than those by the tools with the other rake angles, and they decrease with the increase of the rake angle in the cutting processes with the positive rake angle tools, as shown in Fig. 18. A main reason for these results is that the material removal processes are significantly different when cutting the CFRTPs consisting of 90° fibres with negative, 0° and positive rake angle tools. In terms of negative rake angles, the tool rake face keeps pressing the upper surface of the workpiece during the CFRTP cutting, and the materials from the upper surface to the cutting plane are progressively crushed. The fibres being cut are rarely bent, the deformation of them is hence hard to extend downward into the workpiece along the longitudinal direction and to induce the damage. Therefore, small cutting force and subsurface damage are generated. By contrast, in the cutting process of CFRTPs with the 0° rake angle tool, the fibre direction is parallel to the tool rake face. The whole rake face continuously pushes the fibres and the tool tip can only cut off the fibres after the fibres are bent severely. Under this circumstance, the cutting force and subsurface damage are serious. For the positive rake angle tools, the actions of the tool on the workpiece are detailed in Sect 4.2. The fibres and matrix are fractured at the cutting plane under the push of the tool tip, thus the cutting force and subsurface damage are smaller than those induced by the 0° rake angle tool. In addition, the bigger the tool rake angle, the greater stress could be applied to the materials in the cutting plane. Therefore, the reduced cutting force and subsurface damage are acquired by an increased tool rake angle within the extent of 0°-25°.

5.3 Influence of the Tool Edge Radius

Figure 19 illustrates the predicted subsurface damage distributions in the cutting of CFRTPs with the tools of 25° rake angle and 10 μm, 20 μm and 30 μm cutting edge radii.

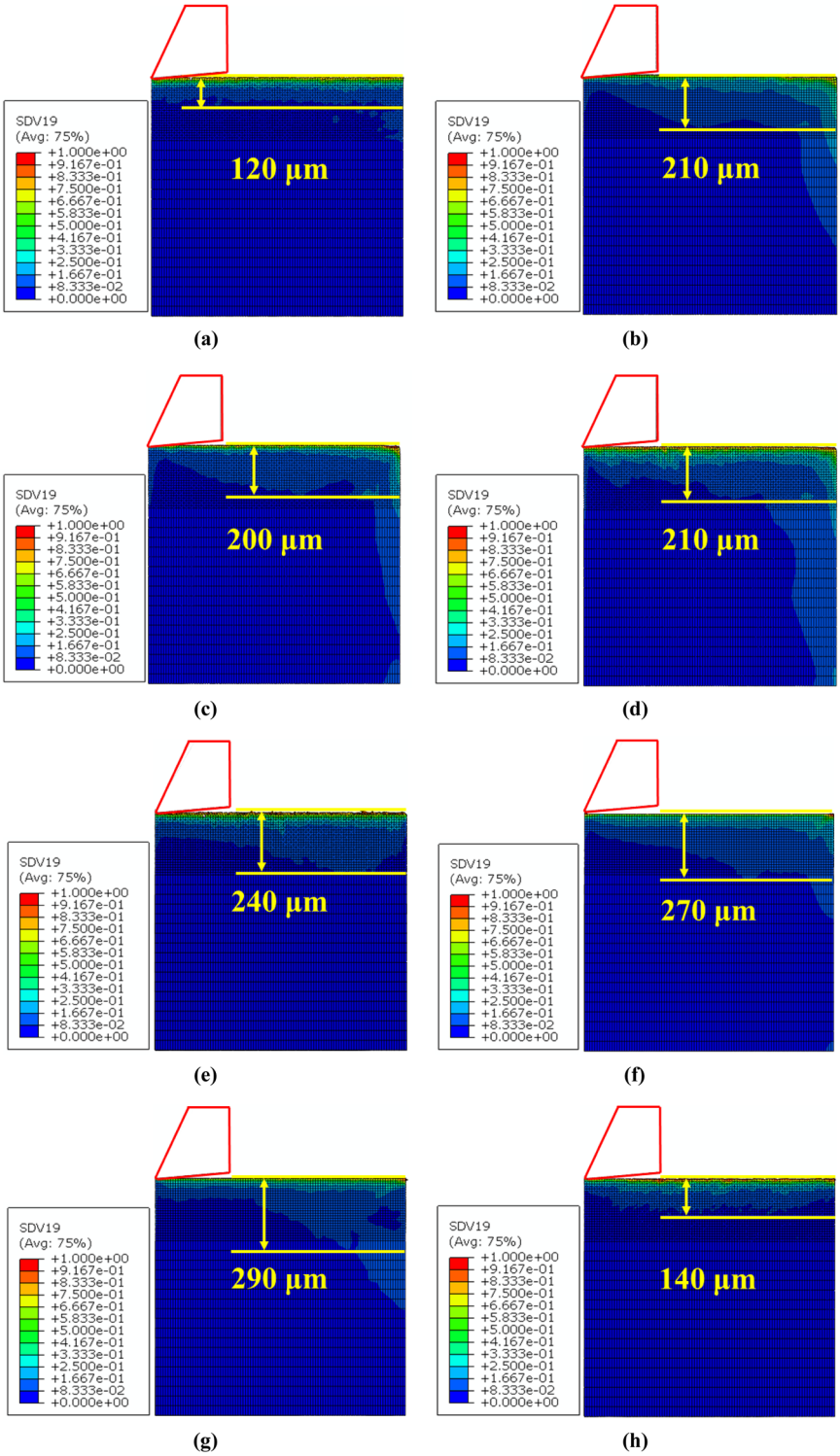
SDV19
(Avg: 75%)
+1.000e+00
+9.167e-01
+8.333e-01
+7.500e-01
+6.667e-01
+5.833e-01
+5.000e-01
+4.167e-01
+3.333e-01
+2.500e-01
+1.667e-01
+8.333e-02
+0.000e+00
120 µm
(a)
210 µm
(b)
200 µm
(c)
210 µm
(d)
240 µm
(e)
270 µm
(f)
290 µm
(g)
140 µm
(h)

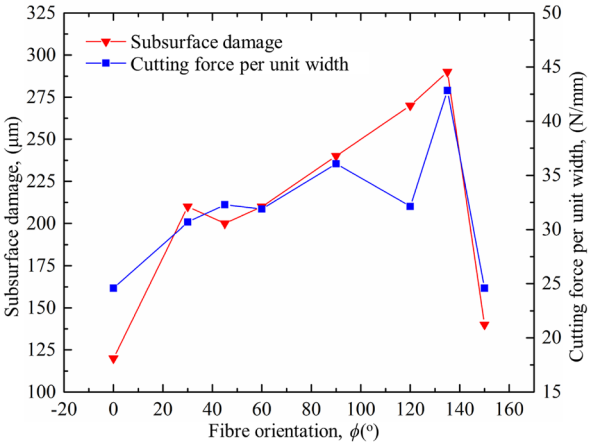

Fig. 16 Variations in the cutting force per unit width and subsurface damage with the fibre orientation

The cutting depth is 50 μm and the workpieces with 90° fibre orientation are adopted in this parametric study. It is indicated from Fig. 20 that the cutting force per unit width and subsurface damage depth increase with the rise of tool edge radius. During the cutting of CFRTPs, the tool with a large edge radius is not easy to concentrate the stress applied to

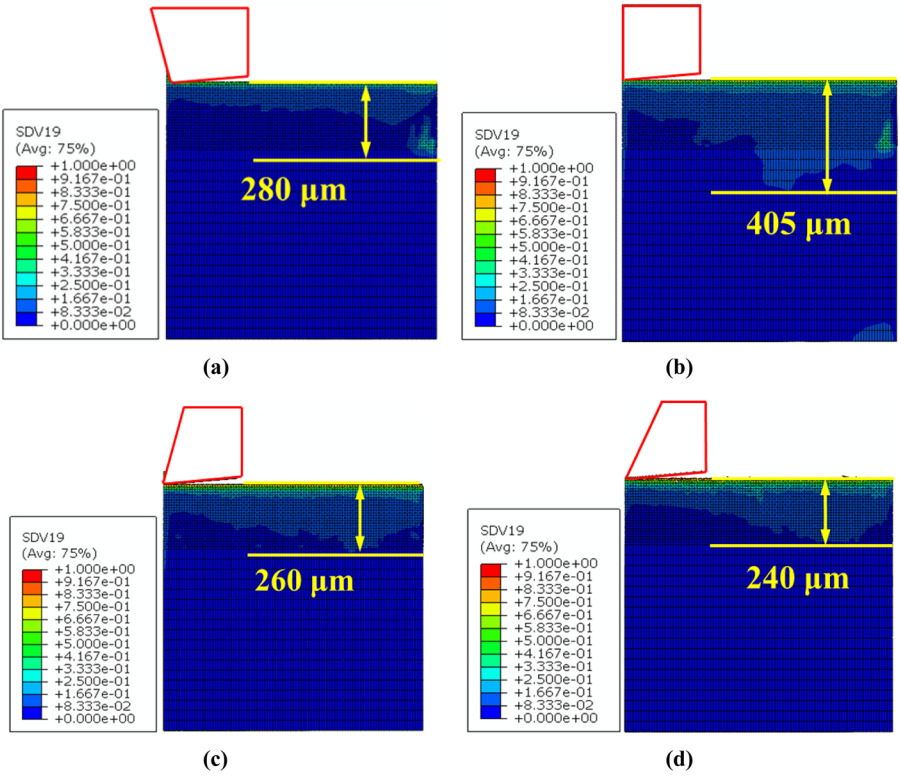

Fig. 17 Subsurface damage under various tool rake angles: **a** -15°; **b** 0°; **c** 15°; **d** 25°

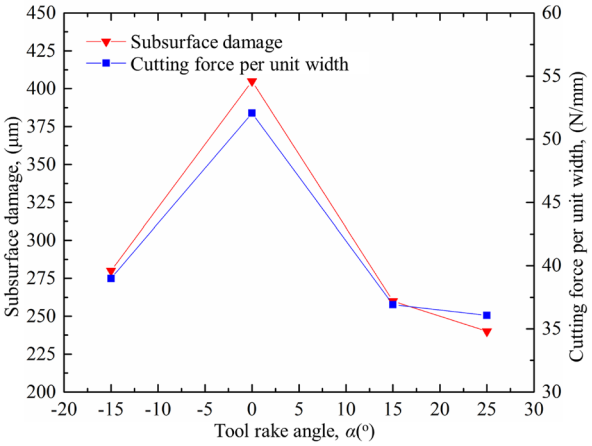

Fig. 18 Variations in the cutting force per unit width and subsurface damage with the tool rake angle

the material at a local point of the material. In this case, the materials, especially the fibres, are difficult to fracture and they keep deformation, which leads to great cutting force and subsurface damage.

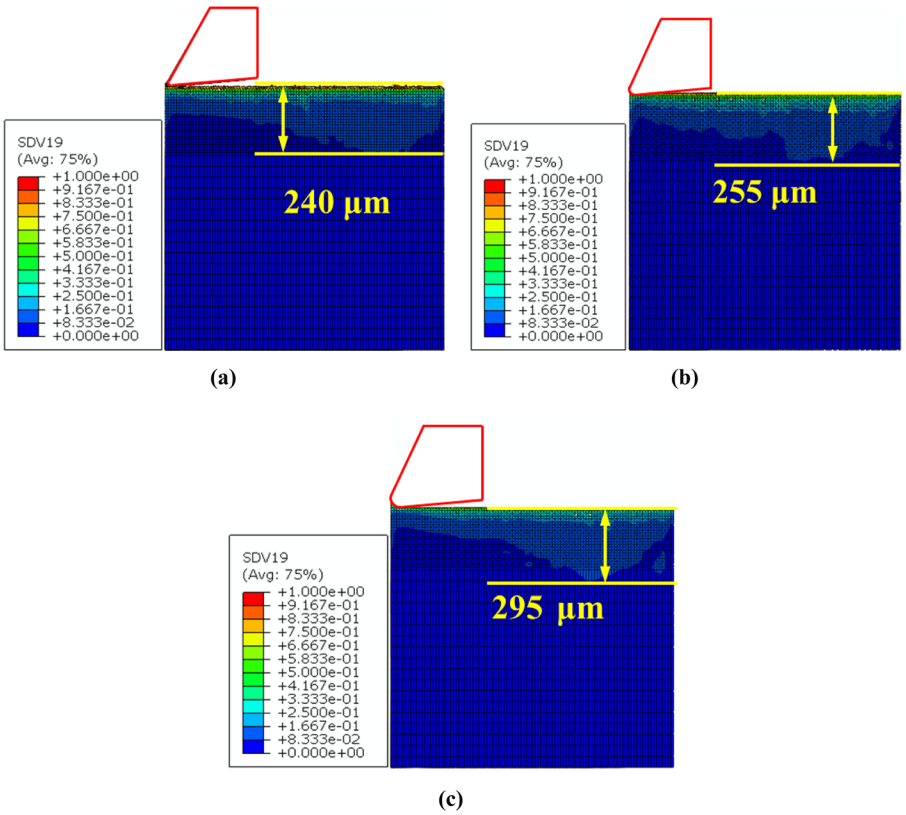

Fig. 19 Subsurface damage under various tool edge radii: (**a**) 10 μm; (**b**) 20 μm; (**c**) 30 μm

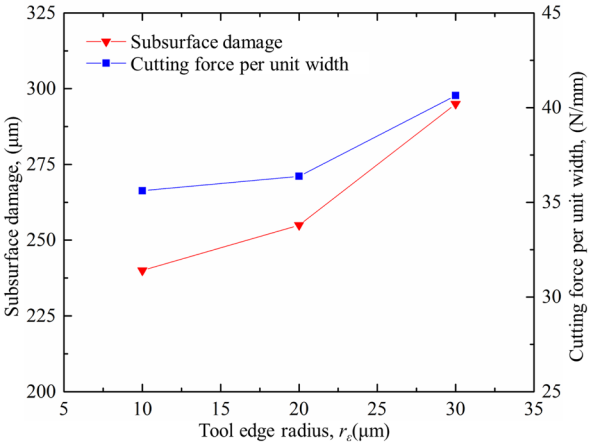

Fig. 20 Variations in the cutting force per unit width and subsurface damage with the tool edge radius

5.4 Influence of the Cutting Depth

Similarly, the cutting depth of 50 μm, 100 μm, 150 μm and 200 μm are numerically investigated for the cutting process of the CFRTP laminates with 90° fibres. The cutting tool is of 25° rake angle and 10 μm cutting edge radius, and the simulation results are presented

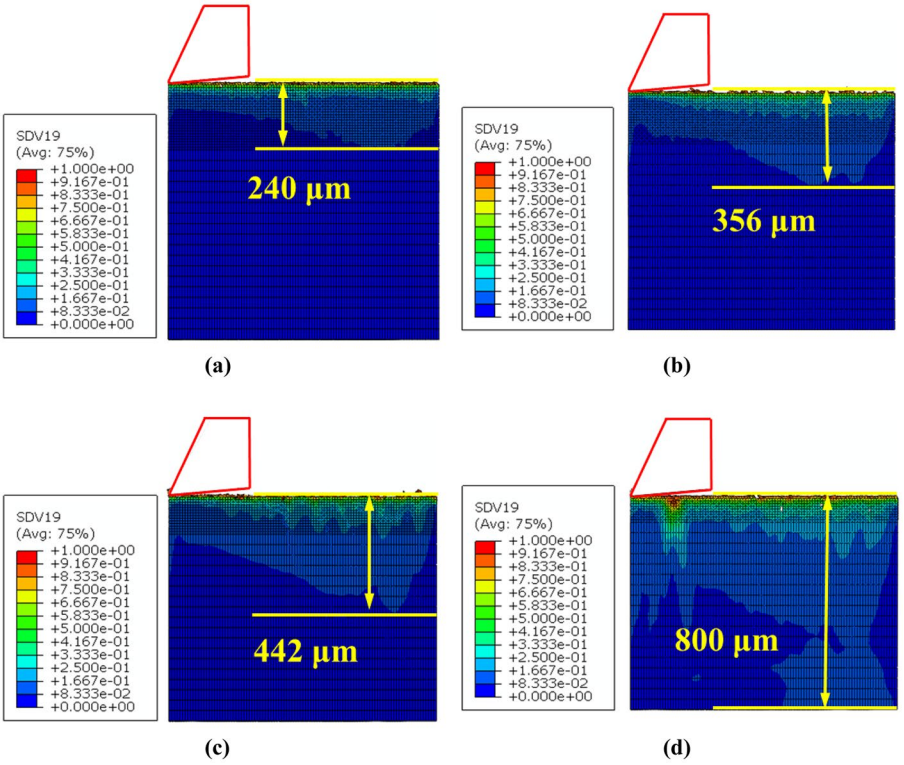

Fig. 21 Subsurface damage under various cutting depths: (a) 50 μm; (b) 100 μm; (c) 150 μm; (d) 200 μm

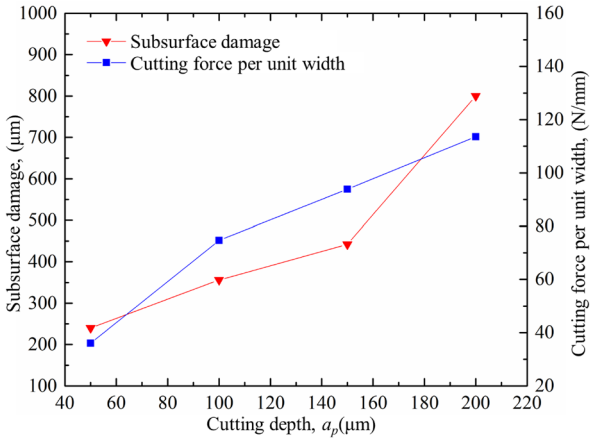

Fig. 22 Variations in the cutting force per unit width and subsurface damage with the cutting depth

in Fig. 21. It could be found that higher cutting forces and subsurface damage are caused by the greater cutting depth (see Fig. 22). For a larger cutting depth, more materials are involved in the cutting process, and more work should be done by the tool to remove the material, thus the cutting force is higher. The great cutting force could cause large deformation of the material, therefore, the enhanced subsurface damage depth is resulted in.

6 Conclusions

In this paper, a novel elastic–plastic damage material model is proposed to numerically simulate the orthogonal cutting of CFRTPs, and to parametrically study the subsurface damage. The mechanical behaviours of the CFRTPs including the plasticity are characterised by utilising a plastic yield function consisting of the various stress components, and the initiation and evolution of the damage with different modes are determined based on the Hashin and Puck criteria and the strain energy density. With this material constitutive model, a 3D FE model for the CFRTP cutting under four typical fibre orientations is developed. The material removal processes, chip morphologies and cutting forces are predicted and compared with the experimental results to verify the FE model and the material constitutive model. Then, the influences of the fibre orientation, tool rake angle, tool edge radius and cutting depth on the subsurface damage depth are assessed using the proposed FE model. Based on the investigations, some conclusions could be obtained as follows:

1. The simulated material removal processes, chip morphologies and cutting forces show good agreement with the experimental outputs. The cutting process and chip morphologies of the CFRTPs change significantly with the variation of the fibre orientation. When the fibre orientation angle is 0°, the simulated cutting force per unit width reaches the minimum value, which is about 25 N/mm, and the chip shape is C-shaped long chips. When the fibre orientation angle is 45°, the chip morphology is curled and long. In 90° and 135° fibre orientations, the chip shape is fragmented. And the maximum cutting force is about 43 N/mm when the fibre orientation is 135°. The error between the simulation cutting forces and experimental cutting forces is less than 20%.

2. The cutting force and subsurface damage depth maintain an approximately growing trend with the increasing of the fibre orientation within the range of 0° to 135°, while a sharp decrease of them occurs at the 150° fibre orientation, where the cutting force decreases to about 25 N/mm, which is close to the cutting force at 0° fibre orientation, and the subsurface damage depth is slightly higher than 0° fibre orientation.
3. The cutting force and subsurface damage induced by the 0° rake angle tool are greater than those by the tools with the other rake angles, and they decrease with the increase of the rake angle in the cutting processes with the positive rake angle tools. The cutting force and subsurface damage keep the same trend with the change of tool rake angle. The cutting force per unit cutting width obtained by simulation analysis reaches the maximum value about 52 N/mm when the rake angle is 0°.
4. The great tool edge radii or cutting depths could lead to a large cutting force per unit width and subsurface damage depth. In the range of greater than 20 μm, the effect of the tool edge radius on the subsurface damage and cutting force is more obvious than that in the range of less than 20 μm.

The proposed model can be used to simulate the chip formation process, chip shape, subsurface damage and cutting force variation under different process parameters in CFRTP orthogonal cutting. The findings are expected to provide guidance for process parameter optimization and tool structure design of CFRTP. Furthermore, the current work will be extended to analyse the drilling or milling process of CFRTP laminates in the near future.

Acknowledgements This work is financially supported by the Major Program of the National Natural Science Foundation of China (Grant No. 52090053), the National Key R&D Program of China (Grant No. 2018YFA0702803), the General Program of the China Postdoctoral Science Foundation (Grant No. 2021M700666), the Liaoning Revitalization Talents Programs (Grant No. XLYC1801008, No. XLYC1902014, and No. XLYCYSZX1901), Science and Technology Innovation Foundation of Dalian (Grant No. 2019CT01 and 2021RD08), the Fundamental Research Funds for the Central Universities (Grant No. DUT21ZD408) and the State Scholarship Fund of China offered by China Scholarship Council (CSC). The authors wish to thank the anonymous reviewers for their comments which lead to improvements of this paper.

Data Availability Statement The datasets generated during the current study are available from the corresponding author on reasonable request.

References

1. Ozen, M., Demircan, G., Kisa, M., Acikgoz, A., Ceyhan, G., Işıker, Y.: Thermal properties of surface-modified nano-Al2O3/Kevlar fiber/epoxy composites. Mater. Chem. Phys. **278**, 125689 (2022)
2. Demircan, G., Kisa, M., Ozen, M., Aktas, B.: Surface-modified alumina nanoparticles-filled aramid fiber-reinforced epoxy nanocomposites: preparation and mechanical properties. Iran. Polym. J. **29**(3), 253–264 (2020)
3. Demircan, G., Kisa, M., Ozen, M., Acikgoz, A.: Quasi-Static Penetration Behavior of Glass-Fiber-Reinforced Epoxy Nanocomposites. Mech. Compos. Mater. **57**(4), 503–516 (2021)
4. Xu, J., Huang, X., Davim, J.P., Ji, M., Chen, M.: On the machining behavior of carbon fiber reinforced polyimide and PEEK thermoplastic composites. Polym. Compos. **41**(9), 3649–3663 (2020)
5. Xu, J., Huang, X., Chen, M., Paulo Davim, J.: Drilling characteristics of carbon/epoxy and carbon/polyimide composites. Mater. Manuf. Process. **35**(15), 1732–1740 (2020)
6. Tan, W., Falzon, B.G., Price, M., Liu, H.: The role of material characterisation in the crush modelling of thermoplastic composite structures. Compos. Struct. **153**, 914–927 (2016)

7. Kim, D., Ramulu, M., Doan, X.: Influence of Consolidation Process on the Drilling Performance and Machinability of PIXA-M and PEEK Thermoplastic Composites. J. Thermoplast. Compos. **18**(3), 195–217 (2005)
8. Hocheng, H., Puw, H.Y.: Machinability of Fiber-Reinforced Thermoplastics in Drilling. J. Eng. Mater. Technol. **115**, 146–149 (1993)
9. Hocheng, H., Pwu, H.Y., Yao, K.C.: MACHINABILITY OF SOME FIBER-REINFORCED THERMOSET AND THERMOPLASTICS IN DRILLING. Mater. Manuf. Process. **8**(6), 653–682 (2007)
10. Rahman, M., Ramakrishna, S., Thoo, H.C.: MACHINABILITY STUDY OF CARBON/PEEK COMPOSITES. Mach. Sci. Technol. **3**(1), 49–59 (1999)
11. Mata, F., Gaitonde, V.N., Karnik, S.R., Davim, J.P.: Influence of cutting conditions on machinability aspects of PEEK, PEEK CF 30 and PEEK GF 30 composites using PCD tools. J. Mater. Process. Tech. **209**(4), 1980–1987 (2009)
12. Kakinuma, Y., Ishida, T., Koike, R., Klemme, H., Denkena, B., Aoyama, T.: Ultrafast Feed Drilling of Carbon Fiber-Reinforced Thermoplastics. Procedia CIRP. **35**, 91–95 (2015)
13. Wang, X., Wang, F., Gu, T., Jia, Z., Shi, Y.: Computational simulation of the damage response for machining long fibre reinforced plastic (LFRP) composite parts: A review. Compos. A. Appl. Sci. Manuf. **143**, 106296 (2021)
14. Wang, F., Wang, X., Yang, R., Gao, H., Su, Y., Bi, G.: Research on the carbon fibre-reinforced plastic (CFRP) cutting mechanism using macroscopic and microscopic numerical simulations. J. Reinf. Plast. Comp. **36**(8), 555–562 (2017)
15. Santiuste, C., Miguélez, H., Soldani, X.: Out-of-plane failure mechanisms in LFRP composite cutting. Compos. Struct. **93**(11), 2706–2713 (2011)
16. Wang, F., Wang, X., Zhao, X., Bi, G., Fu, R.: A numerical approach to analyze the burrs generated in the drilling of carbon fiber reinforced polymers (CFRPs). Int. J. Adv. Manuf. Technol. **106**(7–8), 3533–3546 (2020)
17. Isbilir, O., Ghassemieh, E.: Numerical investigation of the effects of drill geometry on drilling induced delamination of carbon fiber reinforced composites. Compos. Struct. **105**, 126–133 (2013)
18. Wang, F., Gu, T., Wang, X., Jin, X., Zhang, B.: Analysis of Burr and Tear in Milling of Carbon Fiber Reinforced Plastic (CFRP) Using Finite Element Method. Appl. Compos. Mater. **28**(4), 991–1018 (2021)
19. Sun, C.T., Chen, G.: Elastic-Plastic Finite Element Analysis of Thermoplastic Composite Plates and Shells. AIAA J. **30**, 513–518 (1992)
20. Weeks, C.A., Sun, C.T.: MODELING NON-LINEAR RATE-DEPENDENT BEHAVIOR IN FIBER-REINFORCED COMPOSITES. Compos. Sci. Technol. **58**(3–4), 603–611 (1998)
21. Chen, J.F., Morozov, E.V., Shankar, K.: A combined elastoplastic damage model for progressive failure analysis of composite materials and structures. Compos. Struct. **94**(12), 3478–3489 (2012)
22. Chen, J.F., Morozov, E.V., Shankar, K.: Progressive failure analysis of perforated aluminium/CFRP fibre metal laminates using a combined elastoplastic damage model and including delamination effects. Compos. Struct. **114**, 64–79 (2014)
23. Liu, H., Liu, J., Ding, Y., Hall, Z.E., Kong, X., Zhou, J., Blackman, B.R.K., Kinloch, A.J., Dear, J.P.: A three-dimensional elastic-plastic damage model for predicting the impact behaviour of fibre-reinforced polymer-matrix composites. Compos. Part B Eng. **201**, 108389 (2020)
24. Zenia, S., Ayed, L.B., Nouari, M., Delamézière, A.: Numerical prediction of the chip formation process and induced damage during the machining of carbon/epoxy composites. Int. J. Mech. Sci. **90**, 89–101 (2015)
25. Ladeveze, P., Le Dantec, E.: Damage modelling of the elementary ply for laminated composites. Compos. Sci. Technol. **43**, 257–267 (1992)
26. Lubineau, G., Ladevèze, P.: Construction of a micromechanics-based intralaminar mesomodel, and illustrations in ABAQUS/Standard. Comp. Mater. Sci. **43**(1), 137–145 (2008)
27. Yoon, K.J., Sun, C.T.: Characterization of elastic-plastic behavior of AS4/PEEK thermoplastic composite for temperature variation. J. Compos. Mater. **25**(10), 1297–1313 (1991)
28. Liu, H., Falzon, B.G., Li, S., Tan, W., Liu, J., Chai, H., Blackman, B.R.K., Dear, J.P.: Compressive failure of woven fabric reinforced thermoplastic composites with an open-hole: An experimental and numerical study. Compos. Struct. **213**, 108–117 (2019)
29. Falzon, B.G., Liu, H., Tan, W.: Comment on "A tensorial based progressive damage model for fibre reinforced polymers." Compos. Struct. **176**, 877–882 (2017)
30. Zhou, Y., Yazdani Nezhad, H., Hou, C., Wan, X., McCarthy, C.T., McCarthy, M.A.: A three dimensional implicit finite element damage model and its application to single-lap multi-bolt composite joints with variable clearance. Compos. Struct. **131**, 1060–1072 (2015)

31. Rajaneesh, A., Ponthot, J.P., Bruyneel, M.: High velocity impact response of composite laminates using modified meso-scale damage models. Int. J. Impact Eng. **147**, 103701 (2021)
32. Zenia, S., Ayed, L.B., Nouari, M., Delamézière, A.: An Elastoplastic Constitutive Damage Model to Simulate the Chip Formation Process and Workpiece Subsurface Defects when Machining CFRP Composites. Procedia CIRP. **31**, 100–105 (2015)
33. Shi, Y., Swait, T., Soutis, C.: Modelling damage evolution in composite laminates subjected to low velocity impact. Compos. Struct. **94**(9), 2902–2913 (2012)
34. Shi, Y., Pinna, C., Soutis, C.: Modelling impact damage in composite laminates: A simulation of intra- and inter-laminar cracking. Compos. Struct. **114**, 10–19 (2014)
35. Hashin, Z., Rotem, A.: A Fatigue Failure Criterion for Fiber. J. Compos. Mater. **7**(4), 448–464 (1973)
36. Hashin, Z.: Failure Criteria for Unidirectional Fiber Composites. J. Appl. Mech. **47**(2), 329–334 (1980)
37. Puck, A., Kopp, J., Knops, M.: Guidelines for the determination of the parameters in Puck's action plane strength criterion. Compos. Sci. Technol. **62**(3), 371–378 (2002)
38. Puck, A., Schürmann, H.: Failure analysis of FRP laminates by means of physically based phenomenological models. Compos. Sci. Technol. **62**(12–13), 1633–1662 (2002)
39. Puck, A., Schürmann, H.: FAILURE ANALYSIS OF FRP LAMINATES BY MEANS OF PHYSICALLY BASED PHENOMENOLOGICAL MODELS. Compos. Sci. Technol. **58**(7), 1045–1067 (1998)
40. Pinho, S.T., Iannucci, L., Robinson, P.: Physically-based failure models and criteria for laminated fibre-reinforced composites with emphasis on fibre kinking: Part I: Development. Compos. A. Appl. Sci. Manuf. **37**(1), 63–73 (2006)
41. Egan, B., McCarthy, M.A., Frizzell, R.M., Gray, P.J., McCarthy, C.T.: Modelling bearing failure in countersunk composite joints under quasi-static loading using 3D explicit finite element analysis. Compos. Struct. **108**, 963–977 (2014)
42. Ladevèze, P., Allix, O., Deü, J., Lévêque, D.: A mesomodel for localisation and damage computation in laminates. Comput. Method. Appl. M. **183**(1), 105–122 (2000)
43. Tan, W., Falzon, B.G.: Modelling the nonlinear behaviour and fracture process of AS4/PEKK thermoplastic composite under shear loading. Compos. Sci. Technol. **126**, 60–77 (2016)
44. Wang, D., He, X., Xu, Z., Jiao, W., Yang, F., Jiang, L., Li, L., Liu, W., Wang, R.: Study on Damage Evaluation and Machinability of UD-CFRP for the Orthogonal Cutting Operation Using Scanning Acoustic Microscopy and the Finite Element Method. Materials. **10**(2), 204 (2017)
45. Cepero-Mejías, F., Curiel-Sosa, J.L., Zhang, C., Phadnis, V.A.: Effect of cutter geometry on machining induced damage in orthogonal cutting of UD polymer composites: FE study. Compos. Struct. **214**, 439–450 (2019)
46. Mkaddem, A., El Mansori, M.: Finite element analysis when machining UGF-reinforced PMCs plates: Chip formation, crack propagation and induced-damage. Mater. Des. **30**(8), 3295–3302 (2009)
47. Wang, F., Yin, J., Ma, J., Niu, B.: Heat partition in dry orthogonal cutting of unidirectional CFRP composite laminates. Compos. Struct. **197**, 28–38 (2018)
48. Zenia, S., Ben Ayed, L., Nouari, M., Delamézière, A.: Numerical analysis of the interaction between the cutting forces, induced cutting damage, and machining parameters of CFRP composites. Int. J. Adv. Manuf. Technol. **78**(1–4), 465–480 (2015)
49. Benhassine, M., Rivière-Lorphèvre, E., Arrazola, P., Gobin, P., Dumas, D., Madhavan, V., Aizpuru, O., Ducobu, F., Fratini, L., Di Lorenzo, R., Buffa, G., Ingarao, G.: 2D simulations of orthogonal cutting of CFRP: Effect of tool angles on parameters of cut and chip morphology. AIP Conf. Proc. 1960(1) (2018).